

Stratospheric Ozone Response in Experiments G3 and G4 of the Geoengineering Model Intercomparison Project (GeoMIP)

Giovanni Pitari ^a, Valentina Aquila ^b, Ben Kravitz ^c, Shingo Watanabe ^d, Simone Tilmes ^e, Eva Mancini ^a, Natalia De Luca ^a, and Glaucio Di Genova ^a

^a Department of Physical and Chemical Sciences, Università degli Studi de L'Aquila, 67010 Coppito, L'Aquila, Italy (gianni.pitari@aquila.infn.it)

^b Johns Hopkins University, NASA GSFC, Greenbelt, MD 20771, USA (valentina.aquila@nasa.gov)

^c Atmospheric Sciences and Global Change Division, Pacific Northwest National Laboratory, P.O. Box 999, MSIN K9-24, Richland, WA 99352, USA (ben.kravitz@pnnl.gov)

^d Japan Agency for Marine-Earth Science and Technology, Yokohama, Japan (wnabe@jamstec.go.jp)

^e National Center for Atmospheric Research, Boulder, CO 80305, USA (tilmes@ucar.edu)

Corresponding author:

Giovanni Pitari, Università degli Studi de L'Aquila, Department of Physical and Chemical Sciences, Via Vetoio, 67010 Coppito, L'Aquila, Italy; email: gianni.pitari@aquila.infn.it;

phone: +39-0862433074; fax : +39-0862433033

Abstract

Geoengineering with stratospheric sulfate aerosols has been proposed as a means of temporarily cooling the planet, alleviating some of the side effects of anthropogenic CO₂ emissions. However, one of the known side effects of stratospheric injections of sulfate aerosols is a decrease in stratospheric ozone. Here we show results from two general circulation models and two coupled chemistry climate models that have simulated stratospheric sulfate aerosol geoengineering as part of the Geoengineering Model Intercomparison Project (GeoMIP). Changes in photolysis rates and upwelling of ozone-poor air

in the tropics reduce stratospheric ozone, suppression of the NO_x cycle increases stratospheric ozone, and an increase in available surfaces for heterogeneous chemistry modulates reductions in ozone. On average, the models show a factor 20-40 increase of the sulfate aerosol surface area density (SAD) at 50 hPa in the tropics with respect to unperturbed background conditions and a factor 3-10 increase at mid-high latitudes. The net effect for a tropical injection rate of 5 Tg SO_2 per year is a decrease in globally averaged ozone by 1.1-2.1 DU in the years 2040-2050 for three models which include heterogeneous chemistry on the sulfate aerosol surfaces. GISS-E2-R, a fully coupled general circulation model, performed simulations with no heterogeneous chemistry and a smaller aerosol size; it showed a decrease in ozone by 9.7 DU. After the year 2050, suppression of the NO_x cycle becomes more important than destruction of ozone by ClO_x , causing an increase in total stratospheric ozone. Contribution of ozone changes in this experiment to radiative forcing is 0.23 W m^{-2} in GISS-E2-R and less than 0.1 W m^{-2} in the other three models. Polar ozone depletion, due to enhanced formation of both sulfate aerosol SAD and polar stratospheric clouds, results in an average 5% increase in calculated surface UV-B.

1. Introduction

Geoengineering has been proposed as a means of deliberately, temporarily altering the climate to alleviate some of the consequences of anthropogenic greenhouse gas emissions [e.g., *Shepherd et al.*, 2009]. One proposed method involves mimicking a volcanic eruption by injecting sulfate aerosol precursors (e.g., SO_2) into the stratosphere [*Budyko*, 1974; *Crutzen*, 2006]. Large volcanic eruptions are capable of injecting considerable amounts of particles and sulfur gases above the tropopause, causing increases in stratospheric aerosol optical depth, sometimes over one order of magnitude. These volcanic events, the largest most recent ones being Agung, El Chichón, and Pinatubo, in 1963, 1982, and 1991, respectively, can cause substantial surface cooling. The 1991 eruption of Pinatubo, for instance, resulted in reductions in globally averaged surface air temperature by approximately 0.5°C [*Soden et al.*, 2002]. Although volcanic aerosols are episodic, whereas many proposed methods of geoengineering involve sustained injections, they provide important clues as to some of the expected climate response to geoengineering.

Chemical-radiative-dynamical perturbations of the stratosphere following the 1991 eruption of Mt. Pinatubo have been widely studied by the scientific community and reported in the literature.

Nucleation of H₂SO₄ vapour derived from the initial SO₂ plume [Bluth *et al.*, 1992; Read *et al.*, 1993] had produced an optically thick cloud of sulfate aerosols [McCormick and Veiga, 1992; Lambert *et al.*, 1993; Long and Stowe, 1994], which are highly reflective in the visible and UV. This effect is particularly important in the tropics, where the aerosols (depending on the QBO phase) may remain confined for several months after the eruption with relatively high values of optical thickness, as it was the case after Pinatubo [Trepte and Hitchman, 1992]. The radiative feedback of volcanic aerosols is due to additional diabatic heating introduced by: (a) direct interaction with solar and planetary radiation and indirect ozone absorption of the aerosol diffused solar radiation [Pitari, 1993; McCormick *et al.*, 1995]; and (b) changing ozone absorption of incoming solar and outgoing planetary radiation, as a consequence of ozone losses produced by heterogeneous chemistry on volcanic aerosols, perturbed photolysis rates and stratospheric large scale transport [Prather, 1992; Kinne *et al.*, 1992; Schoeberl *et al.*, 1993]. Perturbations of stratospheric tracer species transport may result from dynamical changes due to both local stratospheric heating and climate changes associated to the increasing scattering of incoming solar radiation by the volcanic particles [Hansen *et al.*, 1992; Lacis *et al.*, 1992; Stenchikov *et al.*, 1998; Kirchner *et al.*, 1999]. The stratospheric mean meridional circulation is affected by local aerosol radiative heating (mostly located in the tropical lower stratosphere). The planetary wave propagation in the mid- to high-latitude lower stratosphere is altered as a consequence of changing atmospheric stability due to the climate perturbation. The 1991-1992 time series of the calculated globally averaged net radiative flux change at the tropopause due to aerosols from the Pinatubo eruption [Hansen *et al.*, 1992] shows that the largest forcing occurs during January 1992 (-4.5 W/m^2 , with $\tau = 0.15$); the magnitude of radiative flux changes decreases afterwards with an *e*-folding time of about one year (-1.2 W/m^2 during June 1993). Measurements taken a few months after the Pinatubo eruption revealed a 2-3 K warming in the tropical lower stratosphere [Labitzke and McCormick, 1992; Young *et al.*, 1994] and a 20-25% ozone depletion, with a decrease of about 20 DU of the ozone column in the 16-28 km layer in the tropics during October-November 1991 [Grant *et al.*, 1992; Schoeberl *et al.*, 1993].

In summary, the major effects on stratospheric ozone of large volcanic perturbations of stratospheric aerosols are obtained through: (a) photolysis (of O₂ and O₃, in particular); (b) heterogeneous chemistry on the surface of sulfuric acid aerosols; (c) homogenous chemistry, via temperature changes; (d) heterogeneous chemistry on the surface of polar stratospheric clouds (PSC), via temperature changes and increasing population of sulfate aerosols condensation nuclei; and (e) perturbations of the

stratospheric large scale circulation. Photochemical processes (a)-(c) are mostly relevant for the tropics and mid-latitudes, whereas effect (d) could be important for polar ozone depletion. Although the stratospheric effects due to volcanic eruptions are well studied, the expected effects due to geoengineering have received less attention. *Tilmes et al.* [2008] reported that geoengineering with stratospheric sulfate aerosols could enhance stratospheric ozone destruction and delay the recovery of the Antarctic ozone hole by 30–70 years. Further, the acceleration of ozone loss cycles over the polar regions due to the increase of aerosols may significantly decrease the ozone column and increase erythemal UV by up to 5% in mid and high latitudes and 10% over Antarctica, by mid-century halogen conditions [*Tilmes et al.*, 2012].

The Geoengineering Model Intercomparison Project (GeoMIP) was initiated to determine the robust features of climate model response to four core geoengineering experiments involving uniform solar reduction and stratospheric injections of sulfate aerosol precursors [*Kravitz et al.*, 2011a]. In this study, we investigate the stratospheric ozone response to experiments G3 and G4, with focus on photochemical perturbations. Both of these experiments have a background anthropogenic forcing profile corresponding to RCP4.5 [*Taylor et al.*, 2012]. Beginning in 2020, G3 involves transient stratospheric injections of SO₂ to maintain top of atmosphere net radiation at 2020 levels. G4 involves a constant stratospheric injection rate of 5 Tg SO₂ per year. These simulations are performed for 50 years, after which geoengineering is immediately ceased; the simulations are then run for an additional 20 years to determine the climate response of the termination effect [e.g., *Jones et al.*, 2013]. Because all participating models have performed these same experiments, we can determine the climate model response to these scenarios independent of inter-model differences. In particular, we can determine robust ozone responses in climate models to a sustained layer of stratospheric aerosols

The paper is organized in three sections. Section 2 includes a description of participating models. Section 3 discusses models results regarding stratospheric aerosols (background and GeoMIP perturbations). Section 4 analyzes changes in stratospheric ozone in terms of aerosol induced perturbations in chemical production and loss, vertical profiles, total column, tropopause radiative forcing and surface UV. The main conclusions are summarized in section 5.

2. Description of models

Participating models in this study are the following: ULAQ-CCM (University of L'Aquila Chemistry Climate Model), GISS-E2-R (Goddard Institute for Space Science Model E2), MIROC-ESM-CHEM

(Model for Interdisciplinary Research on Climate), GEOSCCM (Goddard Earth Observing System Chemistry Climate Model). A summary of model runs is presented in Table 1.

The main differences in the treatment of stratospheric aerosols and ozone are summarized here. (a) Aerosol formation starting from oxidation of SO₂ is included in ULAQ-CCM, GISS-E2-R, GEOSCCM; explicit prediction of the aerosol size distribution from microphysical processes is made in ULAQ-CCM; a fixed lognormal size distribution for the dry sulfate aerosol, hydrated depending on the relative humidity, is present in GEOSCCM; MIROC-ESM-CHEM does not calculate aerosol formation in the stratosphere, instead aerosol optical depth (AOD) is specified as a function of latitude, height, month with a fixed lognormal size distribution used in radiative calculations (0.237 μm effective radius); a fixed gamma size distribution for the dry sulfate aerosol, hydrated depending on relative humidity, is used in GISS-E2-R. Aerosol heating rates in solar near-infrared (NIR) and planetary longwave radiation are included in all models. (b) Ozone photochemistry with sensitivity of photolysis to aerosol scattering is in ULAQ-CCM, GISS-E2-R, MIROC-ESM-CHEM; a look-up table for photo-dissociation rates is used in GEOSCCM. (c) Heterogeneous chemical reactions on the surface of sulfate aerosols, with feedback on NO_x chemistry, is included in ULAQ-CCM, MIROC-ESM-CHEM, GEOSCCM; it is not included in GISS-E2-R and in specific sensitivity runs of ULAQ-CCM. The acronym ‘nhc’ used throughout the paper stands for ‘no heterogeneous chemistry on stratospheric sulfate aerosol’.

2.1 ULAQ-CCM

The University of L’Aquila model is a low-resolution global scale climate-chemistry coupled model (ULAQ-CCM) extending from the surface to the mesosphere (0.04 hPa); model features are described by *Pitari et al.* [2002], *Eyring et al.* [2006], and *Morgenstern et al.* [2010]. After participation in CCMVal-2, some important updates have been made to the model: (a) increase of horizontal and vertical resolution, now T21 with 126 log-pressure levels (approximate pressure altitude increment of 568 m); (b) inclusion of a parameterization for the formation of upper tropospheric cirrus cloud ice particles [*Kärcher and Lohmann, 2002*]; (c) update of species cross sections using recommendations by *Sander et al.* [2011] and Schumann-Runge bands treatment following the parameterization of *Minschwaner et al.* [1993] based on fixed-temperature opacity distribution function formulation; (d) upgrade of the radiative transfer code for calculations of photolysis, solar heating rates and top-of-

atmosphere radiative forcing. The oceanic surface temperature is assimilated from the Hadley Centre for Climatic Prediction and Research [Rayner *et al.*, 2003]; the parameterization of periodic natural forcings (solar cycle, quasi-biennial oscillation) is included on-line. The chemistry module is organized with all medium and short-lived species grouped in the families O_x , NO_y , NO_x , CHO_x , Cl_y , Br_y , SO_x , and the module also includes aerosols. In total there are 40 transported species, 26 species at photochemical equilibrium and 57 size categories for aerosols. The model includes the major components of stratospheric and tropospheric aerosols (sulfate, carbonaceous, soil dust, sea salt, PSCs). The size distributions of sulfate (both tropospheric and stratospheric) and PSC particles are calculated using an interactive and mass conserving microphysical code for aerosol formation and growth, including a gas-particle conversion scheme. New sulfuric acid particles are formed via homogeneous nucleation, followed by coagulation and condensation growth; stratospheric aerosols are lost via evaporation in the upper stratosphere and downward transport and sedimentation into the troposphere. For the GeoMIP simulations, SO_2 was injected throughout the altitude range of 18–24 km at 0° longitude on the equator. Lower stratospheric denitrification and dehydration are calculated using the predicted size distribution of PSC particles; heterogeneous reactions on sulfate and PSC aerosols are included in the chemistry module [Pitari *et al.*, 2002], with the hydrolysis of N_2O_5 and $BrONO_2$ being the two most important reactions on the surface of stratospheric sulfuric acid aerosols. The updated radiative transfer module, operating on-line in the ULAQ-CCM, is a two-stream delta-Eddington approximation model [Toon *et al.*, 1989], used for chemical species photolysis rate calculation in ultraviolet (UV)–visible (VIS) wavelengths and for solar heating rates and radiative forcing in UV–VIS–near-infrared (NIR) bands. Top-of-atmosphere solar fluxes are taken from SUSIM-SL2 and LOWTRAN7 and are integrated on the wavelength bins used in the model, of which there are 150 in the UV and visible range and 100 in the NIR range, covering the solar spectrum from Lyman- α up to 7 μm . Sun–earth distance is calculated daily as a function of orbit eccentricity and the solar cycle is included. Sphericity is treated by means of Chapman functions [Dahlback and Stamnes, 1993]. Refraction is taken into account with an iterated ray-tracing technique in a simple exponential refraction model. Optical depths take into account Rayleigh scattering, radiation absorption from O_3 , O_2 , NO_2 , SO_2 , H_2O , CO_2 and scattering/absorption from aerosol particles. Planetary radiation heating rates and top of atmosphere/tropopause forcings are calculated including absorption/emission by CO_2 (15 μm band), O_3 (9.6 μm band), H_2O and aerosols, using well tested absorptivity formulas through a correlated-k method. Aerosol extinction values are passed daily from the ULAQ-CCM aerosol module to the radiative transfer module, with appropriate wavelength-dependent values of extinction

coefficient, asymmetry factor and single scattering albedo, given the calculated size distribution of the particles. Surface albedo is taken from MERRA 2D hourly averaged data. The ULAQ model calculations of photolysis rates and surface and top-of-atmosphere radiative fluxes have been validated in the framework of CCMVal and AEROCOM inter-comparison campaigns [Chipperfield and Liang *et al.*, 2013; Randles *et al.*, 2013].

2.2 GISS-E2-R

GISS-E2-R is a fully coupled atmosphere-ocean general circulation model, developed by the National Aeronautics and Space Administration's (NASA) Goddard Institute for Space Studies (GISS), which is a contributor to the Coupled Model Intercomparison Project Phase 5 (CMIP5) [Schmidt *et al.*, 2006; Taylor *et al.*, 2012]. The atmospheric model has a horizontal resolution of 2° latitude by 2.5° longitude and 40 vertical layers extending through the mesosphere (model top of 0.1 hPa). It is coupled to the Russell ocean model [Russell *et al.*, 1995] which has horizontal resolution of 1° latitude by 1.25° longitude and 32 vertical layers. The version discussed here was run with full stratospheric chemistry, involving 113 fully resolved reactions. Photolysis in the stratosphere is included and varies dynamically as a function of temperature, pressure, solar output, cloudiness, albedo, and ozone concentration. Ozone and methane are computed at the model's resolution and are radiatively interactive with model tracers, i.e., they modify heating rates and are chemically active. Formation of sulfate aerosols is specified by a reaction rate in which an aerosol dry radius is specified, as described by Koch *et al.* [2006]. The aerosols then grow hygroscopically according to ambient relative humidity per the formulas of Tang [1996]. In this study, the aerosol dry radius is specified to be 0.35 μm , which is the same specification as was used by Robock *et al.* [2008] in their simulations of the 1991 eruption of Mount Pinatubo and results in an approximately Pinatubo-sized aerosol in simulations of volcanic eruptions, per GeoMIP specifications [Kravitz *et al.*, 2011b]. SO₂ was injected throughout the altitude range of 16–25 km at 0° longitude on the equator. The aerosols are radiatively active tracers and are advected within the model via the general circulation. Stratospheric sulfate aerosols injected into the tropical lower stratosphere have an *e*-folding lifetime of approximately 12 months.

2.3 MIROC-ESM-CHEM

MIROC-ESM-CHEM is an Earth System Model (ESM) that has been developed based on a global climate model MIROC (Model for Interdisciplinary Research on Climate) consisting of coupled atmosphere, ocean, sea ice, river, and land surface models. The details of MIROC-ESM-CHEM model and the base (RCP4.5) simulation settings have been documented in *Watanabe et al.* [2011a] and *Watanabe et al.* [2011b], respectively. The atmosphere model of MIROC-ESM-CHEM has a T42 horizontal resolution (approximately 300 km grid spacing), and contains 80 vertical layers from the surface to a height of about 85 km. The model predicts effects of the solar cycle, QBO, and ENSO online. The model considers the direct and indirect effects of tropospheric aerosols, while treatments of the stratospheric aerosols are separated from the tropospheric one as is outlined below.

In the base simulation, a zonally averaged stratospheric aerosol AOD is provided to the model's radiation module as a function of latitude, altitude and month following *Sato et al.* [1993], which is exponentially reduced after 1998 with one year relaxation time toward a background value of 10^{-4} . In G4, we used similar latitude- altitude- and monthly data of AOD but provided by GeoMIP for models which do not simulate formation of the stratospheric sulfate aerosols from SO_2 gas [*Kravitz et al.*, 2011b]. In radiation calculations, a constant effective radius of $0.237 \mu\text{m}$ is used in both the base and G4 runs. More details of the radiation calculations are discussed by *Watanabe et al.* [2011b].

The atmospheric chemistry module of MIROC-ESM-CHEM predicts the system of tropospheric chemistry (O_x - HO_x - NO_x - CO - CH_4 - VOCs: Volatile Organic Compounds) as well as major chlorine and bromine compounds (Cl_y and Br_y) that are important for the simulation of stratospheric ozone [*Watanabe et al.*, 2011a]. Parameterizations for liquid and solid particles in the stratosphere are included to calculate heterogeneous reactions on liquid sulfate aerosols (including the hydrolysis of N_2O_5 and BrONO_2) and PSCs [e.g., *Carslaw et al.*, 1995; *Hanson and Mauersberger*, 1988]. SADs of PSCs are diagnosed as a function of the predicted temperature and mixing ratio of H_2O and HNO_3 . On the other hand, SAD of liquid sulfate aerosols (S) in the stratosphere including those background and volcanic aerosols are given as an external forcing in this study. Namely, S (in $\mu\text{m}^2\text{cm}^{-3}$) is approximately diagnosed in the heterogeneous chemistry package based on the AOD data:

$$S = 4c \frac{\Delta\tau}{\Delta z} \frac{1}{\varepsilon},$$
 where c is a constant for unit conversion (10^{10}), $\Delta\tau$ is τ in a certain model layer at a certain location, Δz is a thickness of the model layer (m), and ε is a prescribed constant representing mean efficiency of scattering due to the sulfate aerosols (assumed to be 2). This relationship is derived through a combination of several basic and approximated equations, and gives S distribution which

resembles to observations [e.g., *Thomason et al.*, 1997b], via solving out n and σ from the following: $S = 4\pi \cdot r^2 n$, $\Delta\tau = n\sigma\Delta z$, and $\sigma = \varepsilon\pi \cdot r^2$, where n , r and σ are the number density, effective radius, and a mean scattering cross section of sulfate aerosols in the model layer.

2.4 GEOSCCM

The Goddard Earth Observing System Chemistry Climate Model (GEOSCCM) used for the GeoMIP simulations couples the Goddard Earth Observing System, version 5 (GEOS-5) [*Rienecker et al.*, 2008] general circulation model to the Georgia Institute of Technology-Goddard Global Ozone Chemistry Aerosol Radiation and Transport (GOCART) module [*Chin et al.*, 2000, *Colarco et al.*, 2010] and a stratospheric chemistry module [*Pawson et al.*, 2010].

GEOS-5 uses a finite volume dynamical core [*Lin*, 2004] combined with a physics package that describes moist processes, radiation, turbulent mixing and surface processes. Convection is parameterized using the relaxed Arakawa-Schubert (RAS) scheme [*Moorthi and Suarez*, 1992], and is combined with a prognostic cloud scheme. The boundary layer turbulent mixing is parameterized with the schemes by *Louis et al.* [1982] and *Lock et al.* [2000] for stable and unstable situations, respectively. The land surface model is composed of a catchment-based hydrological model [*Koster et al.*, 2000] and a multilayer snow model [*Stieglitz et al.*, 2001]. The radiative transfer model consists of a solar radiation model [*Chou and Suarez*, 1999] and a thermal radiation model [*Chou et al.*, 2001]. The solar radiation model includes absorption due to water vapor, O₃, O₂, CO₂, clouds and aerosols. The thermal radiation model includes absorption by water vapor, CO₂, O₃ and most of the minor trace gases, as well as clouds and aerosols. GOCART includes a parameterization of the chemical production of SO₄ aerosol from oxidation of dimethyl sulfide (DMS) by OH during day and NO₃ during night, and from oxidation of SO₂ by OH in the gas phase and by H₂O₂ in the aqueous phase.

The surface area density of stratospheric aerosols is used in the heterogeneous chemistry module. GEOSCCM calculates the aerosol SAD from the concentration of SO₄ assuming that the dry stratospheric sulfate aerosol particles are lognormally distributed with modal radius equal to 0.35 μm and standard deviation 1.6. These values have been chosen within the observed range [e.g. *Bingen et al.*, 2004] and result in good agreement with observations of the period after the eruption of Mount

Pinatubo [Aquila *et al.*, 2012]. The dry stratospheric aerosol is hydrated depending on the ambient relative humidity following Petters and Kreidenweis [2007].

A similar version of GEOSCCM has been evaluated by Aquila *et al.* [2012] and Aquila *et al.* [2013]. Respect to Aquila *et al.* [2013], the version of GEOSCCM used in this work includes the coupling between aerosol and heterogeneous chemistry through the aerosol SAD, different parameters for the aerosol size distribution to reach a better agreement with observations, and an internal mechanism for the generation of the QBO [Molod *et al.*, 2012]. GEOSCCM is used in this work to perform only G4 simulations and the relative control simulations. Here, 5 Tg per year of SO₂ is continuously injected at the equator at 0° longitude. The injection is uniform between 16 km and 25 km altitude. The transformation of SO₂ into sulfate aerosol is calculated by GOCART using climatological oxidant fields [Chin *et al.*, 2000].

GEOSCCM does not directly simulate the stratospheric background aerosol. In the RCP4.5 control simulations, GEOSCCM prescribes aerosol SAD from the Stratospheric Aerosol Measurement II (SAM II) and Stratospheric Aerosol and Gas Experiment (SAGE) data (Eyring *et al.*, 2008) relative to the year 1979 – a period when the stratospheric aerosol layer was relatively unperturbed (Thomason *et al.*, 1997a)- for the purpose of calculating the heterogeneous chemistry. The radiative effect of the background aerosol, however, is not included in this simulation. In the G4 simulations the SAD calculated from the simulated sulfate aerosol mass is added to the prescribed background SAD.

The model resolution used for these simulations is 2.0° latitude by 2.5° longitude and 72 vertical hybrid levels up to 0.01 hPa. The model is forced with sea surface temperatures and sea ice concentrations from RCP4.5 future simulations performed with the Community Earth System Model (CESM) [Gent *et al.*, 2011].

3. Stratospheric aerosols

Explosive volcanic perturbations and potential stratospheric sulfate aerosol geoengineering may act as large stratospheric sources of SO₂, producing transient or steady state major increases of the stratospheric sulfate aerosol number, mass and surface area densities, as well as solar radiation extinction and optical depth; this can result in significant changes of the particle size distribution respect to the stratospheric background aerosol [Deshler *et al.*, 1992; Thomason *et al.*, 1997b]. These

large aerosol perturbations directly impact the radiation budget at the surface and at the top of atmosphere, as well as the hydrologic cycle and tropospheric and stratospheric ozone [e.g., *Robock, 2000; Robock et al., 2008; Tilmes et al., 2008*]. To understand the stratospheric ozone anomaly induced by a perturbation of the stratospheric sulfate aerosol burden, we must first establish the aerosol size distributions and surface area. For example, larger aerosols will have a greater infrared radiative effect with respect to small aerosol, causing increased stratospheric heating and hence greater radiative-chemical-dynamical changes. A change in surface area density will change the amount of surface available for heterogeneous chemistry.

Background stratospheric sulfate aerosols are either formed locally by OH oxidation of SO₂ or transported upward from the troposphere through the tropical tropopause layer (TTL), although the latter process is largely limited by upper tropospheric formation of cirrus ice particles via homogeneous freezing on sulfate aerosols [*Hendricks et al., 2011*]. Stratospheric SO₂, in turn, originates either from convection of SO₂ from the boundary layer to the TTL, followed by vertical advection from the TTL, or from local photochemical production, following photolysis of OCS [*Pitari et al., 2002; Weisenstein et al., 2006*]. Sulfuric acid produced at the end of the SO₂ oxidation chain forms aerosol particles via homogeneous nucleation (and to a lesser extent via heterogeneous nucleation of carbonaceous particles transported from the troposphere). The particle size distribution is determined by these and other microphysical processes, such as condensational growth, coagulation, gravitational settling and evaporation in the upper stratosphere. The main sink for stratospheric sulfate aerosols is the mid-high latitude downward transport towards the troposphere coupled to gravitational sedimentation, with an average lifetime of about one year [*Weisenstein et al., 2006*].

Model predictions of AOD perturbations in the GeoMIP experiments are presented in Fig. 1. G4 imposes the amount of SO₂ injected mass flux (5 Tg/year): inter-model differences arise from longer or shorter stratospheric aerosol lifetimes, which in turn are produced by inter-model differences of the tropical pipe isolation and net mixing with extratropics, as well as differences of the Brewer-Dobson circulation strength and its potential modulation by stratospheric aerosol heating and QBO. The aerosol particle size distribution also plays an important role, by affecting the gravitational sedimentation rate. On the other hand, G3 imposes the conservation of the top-of-atmosphere radiative forcing (TOARF) during the GeoMIP time span (2020-2070). Assuming that the net change of the TOARF in these 50 years is of the order of 2 W/m² [*Meinshausen et al., 2011*], the imposed stratospheric mass flux of SO₂ in G3 may have large variations among the models. This variation depends mostly on the treatment of

the aerosol effects on other atmospheric processes (e.g., O_3 , tropospheric cloudiness, albedo), since the direct aerosol equivalent-albedo effect is only slightly affected by the model-predicted aerosol size [Lacis *et al.*, 1992].

In the present study, G3 with interactive ozone is simulated by two models (ULAQ-CCM and GISS-E2-R), both of which include explicit aerosol feedbacks with ozone photochemistry but not aerosol-cloud interactions. Model predicted aerosol optical depth for G3 is approximately a factor of 5 larger in ULAQ-CCM than GISS-E2-R. This is in part due to a low responsiveness of GISS-E2-R to CO_2 changes as compared to several other models participating in CMIP5 [e.g., Kravitz *et al.*, 2013], and consequently to a lower TOARF to be compensated by the geoengineering aerosol. The two models agree quite well in the predicted globally-averaged AOD in G4, where the SO_2 mass flux is imposed, independent of its net effect on the radiative forcing.

Panels (d, e) of Fig. 1 show that the AOD latitudinal dependence is rather different among models that predict aerosols from the SO_2 injection: GEOSCCM and ULAQ-CCM have similar aerosol effective radii (Table 2) and then comparable stratospheric aerosol loss due to sedimentation. This, coupled to a good tropical pipe isolation [e.g. Strahan *et al.*, 2011; Chipperfield and Liang *et al.*, 2013], produces an effective aerosol confinement in the tropics, with a clear equatorial AOD maximum and comparable globally-averaged AOD. On the other hand, the GISS-E2-R latitudinal distribution shows a much faster aerosol dispersion towards mid-high latitudes (to be associated to a more efficient sub-tropical horizontal air mixing in the lower stratosphere), thus producing a tropical minimum of the AOD. The globally-averaged value, however, is comparable and even higher than that of GEOSCCM and ULAQ-CCM, due to the slower sedimentation loss produced by the smaller particle size (Table 2).

The growth of stratospheric aerosol particles, produced by both transient or sustained SO_2 injections, modifies the particle size distribution shape leading to significantly larger effective radii with respect to normal background conditions of the stratosphere. This is highlighted both in direct satellite measurements of aerosol extinction after a major volcanic eruption [Thomason *et al.*, 1997b] and in global modeling studies [Weisenstein *et al.*, 2006; Heckendorn *et al.*, 2009]. Owing to their large size, these particles have a reduced albedo and a faster sedimentation rate, with a net reduction of the stratospheric lifetime: both effects end up limiting the cooling potential with respect to stratospheric background aerosols. In addition, the increasing particle size favors the absorption of infrared radiation both in the solar NIR and planetary spectra, leading to larger additional tropical heating rates. This

local radiative perturbation may have a potential increasing impact on tropical upwelling and (by continuity) on the extra-tropical downwelling, acting again to reduce the lifetime of stratospheric aerosols. Table 2 shows that two of the three models that form aerosols from the stratospheric SO₂ injection actually predict an increase of the effective radius in G4 with respect to RCP4.5 (i.e. ULAQ-CCM and GISS-E2-R), and two models calculate a G4 perturbed effective radius close to SAGE-II observations after the Pinatubo eruption (ULAQ-CCM and GEOSCCM). The effective radius is the radiative-effective aerosol dimension, determining the efficiency of radiation scattering and absorption. Inter-model differences in Table 2 need to be taken into account to evaluate the GeoMIP aerosol impact on radiative processes, such as photolysis and stratospheric heating rates.

The SAGE-II measured extinction ratio between visible and NIR wavelength channels (i.e. 0.525 and 1.02 μm , respectively) is a good measure of the aerosol size distribution shape and its modifications produced by changes in the local sulfate productions rate from OH oxidation of SO₂ [Weisenstein *et al.*, 2006]. As shown in Fig. 2, this ratio is close to unity when the effective radius is close to 0.6 μm and about 3 for $r_{\text{eff}} = 0.2 \mu\text{m}$. The ULAQ-CCM is the only model included in this paper with explicit aerosol microphysics and calculates the time behavior of the sulfate aerosol size distribution as a function of stratospheric SO₂, OH, and large scale transport. Its predictions in terms of the extinction ratio (and hence of the aerosol size distribution shape) are shown in Fig. 2 to be in good agreement with SAGE-II observations, for both background and perturbed conditions (G4 and Pinatubo). Panel (b) of Fig. 2 compares directly the ULAQ-CCM calculations of the aerosol size distribution for background and G4 conditions, confirming the previous findings.

Aerosol SAD changes are presented in Fig. 3-4: these are important for assessing changes in heterogeneous chemical reactions in the stratosphere, particularly NO_x and other O₃ chemical precursors (Cl_x, Br_x). The models use different approaches for calculating the SAD. ULAQ-CCM calculates directly the geometric surface area starting from the predicted aerosol size distribution. GEOSCCM calculates the SAD from the sulfate aerosol mass concentration, assuming that the dry stratospheric sulfate aerosol is log-normally distributed with modal radius 0.35 μm and standard deviation 1.59. This dry size distribution is hydrated depending on the relative humidity following Petters and Kreidenweis [2007]. MIROC-ESM-CHEM approximately calculates the SAD from the prescribed AOD distribution, as mentioned in Section 2.3. Model results are also validated with SAGE-II data, for both volcanically quiet and perturbed conditions. Although some differences are present in the latitudinal distribution of the aerosol SAD, all three models are well consistent with the

reported SAGE-II derived SAD values for background and post-Pinatubo conditions. It should be noted that the average sulfate mass loading above the tropopause is comparable in G4 steady-state conditions (4.83 ± 0.06 Tg-S) with respect to April 1992 – March 1993 post-Pinatubo conditions (4.7 ± 0.6 Tg-S); these mass burden estimates are calculated as an average from ULAQ-CCM and GEOSCCM time-dependent simulations. This makes possible and meaningful to use the indirect G4 SAD validation with SAGE-II derived values from April 1992 to March 1993. On average, the three models show a factor 20-40 increase of the tropical aerosol SAD at 50 hPa with respect to RCP4.5 (with ULAQ-CCM on the upper limit), and a factor 3-10 increase at mid-high latitudes (with GEOSCCM on the lower limit). These large sulfate aerosol SAD increases greatly affect the stratospheric NO_x - HO_x - Cl_x - Br_x chemistry [Fahey *et al.*, 1993] by converting more NO_x into HNO_3 and by increasing the amount of HO_x and reactive Cl-Br. The balance of these catalytic cycle changes may enhance or limit the stratospheric ozone destruction depending on latitude, altitude and on the (time-dependent) total stratospheric amount of inorganic Cl_y and Br_y .

4. Stratospheric ozone

The increase in stratospheric sulfate concentrations affects ozone via the enhancement of heterogeneous chemistry on the larger aerosol surface area density [e.g. Brasseur and Granier, 1992], changes in photolysis rates due to the increased aerosol optical thickness [Kinne *et al.*, 1992], and modifications of the atmospheric dynamics due to aerosol-ozone perturbations of the stratospheric heating rates [Pitari and Rizi, 1993; Aquila *et al.*, 2013], which are coupled to altered amplitude and propagation of planetary waves [Pitari and Mancini, 2002]. The temperature perturbations in the middle stratosphere may also affect the homogeneous chemical reaction rates with pronounced temperature dependence, such as $\text{O}+\text{O}_3$ and $\text{NO}+\text{O}_3$. ULAQ-CCM and MIROC-ESM-CHEM include all of these effects. GEOSCCM includes the ozone perturbations due to heterogeneous and homogeneous chemistry and to atmospheric dynamics, but not changes in photolysis rates. GISS-E2-R includes the ozone perturbations due to changes in photolysis rates, atmospheric dynamics and homogeneous chemistry, but not those due to heterogeneous chemistry on the sulfate aerosol surface. However, GISS-E2-R does include treatments of heterogeneous chemistry in polar stratospheric clouds, which is particularly relevant for Antarctic ozone changes.

The models consistently simulate an enhancement of the heterogeneous chemical reactions in the GeoMIP experiments, with a direct significant depletion of stratospheric NO_x , as reported in the literature after major volcanic eruptions [e.g. *Johnston et al.*, 1992; *Koike et al.*, 1994]. Figure 5 shows the NO_x ($\text{NO} + \text{NO}_2$) mixing ratio changes for G4 during the central decade 2040-2050 (GISS-E2-R is not pictured in Fig. 5 because it does not include heterogeneous chemistry on the particle surfaces). All models calculate a decrease in NO_x between 100 hPa and 5 hPa altitude in the tropics (20S-20N) and mid-latitudes (30S-50S and 30N-50N), of the order of 0.5-1 ppbv in the 10-50 hPa layer. Above 10 hPa the models show a small increase of NO_x (0.2 to 0.5 ppbv at 2 hPa). This is most likely due to the fact that both O_3 and NO_2 photolysis decrease as a consequence of the aerosol scattering (see ahead Fig. 7), so that (in addition to its enhanced heterogeneous chemical loss) less NO is available as sink for NO_y through UV photolysis. This effect is less evident in GEOSCCM, which does not take into account the aerosol impact on photolysis.

4.1 Changes in the vertical profile of ozone

A comparison of O_3 production/loss terms per chemical family in G4 respect to the base case has been made with the ULAQ model output. In order to highlight the direct impact of precursors changes on the ozone chemistry, the net chemical production term ($P-L[\text{O}_3]$) has been compared between the two simulations by keeping $[\text{O}_3]$ fixed at the RCP4.5 value, which means that a comparison of O_3 production (P) and loss frequency (L) terms is actually made (ΔP and $[\text{O}_3] \cdot \Delta L$ are plotted in Fig. 6). The ULAQ-CCM calculates an increase in net ozone production rate in the tropics between 30 hPa and 7 hPa for the decade 2040-2050 (on average $+0.4 \cdot 10^5 \text{ cm}^{-3} \text{ s}^{-1}$), and a decrease at all other tropical stratospheric altitudes (Fig. 6a). The significant NO_x decrease discussed in Fig. 5 drives most of the chemical changes, by decreasing the O_3 destruction from $\text{NO}_2 + \text{O}$ and the O_3 production from $\text{NO} + \text{HO}_2$ and $\text{NO} + \text{CH}_3\text{O}_2$. This results in a net increase of the ozone production term from the NO_x cycles up to about 7 hPa (with a peak increase of $+1.3 \cdot 10^5 \text{ cm}^{-3} \text{ s}^{-1}$ at 20 hPa).

Indirectly, the NO_x change produced by the enhanced heterogeneous chemical reactions on sulfate aerosol SAD forces an increase of the O_3 loss by HO_x , Cl_x and Br_x catalytic cycles (due to the decreasing loss of OH from $\text{OH} + \text{NO}_2$ and the decreasing amounts of chlorine and bromine nitrates); a peak increase of $-0.6 \cdot 10^5 \text{ cm}^{-3} \text{ s}^{-1}$ for these loss terms is calculated at 20 hPa. The perturbation to the O_2 photolysis rate (see Fig. 7a) dominates below 50 hPa due to the UV screening effect by the aerosols; the ozone increase forced by the NO_x cycle perturbation in the 7-30 hPa layer has a feedback on the O_2

photolysis (Fig. 7a), thus decreasing the O_3 production from JO_2 in this same layer ($-0.4 \cdot 10^5 \text{ cm}^{-3} \text{ s}^{-1}$, on average). Changes of ozone production/loss above 7 hPa ($-0.2 \cdot 10^5 \text{ cm}^{-3} \text{ s}^{-1}$, on average) result from partially compensating effects of decreasing $O(^3P)$ from O_3 photolysis (Fig. 7b) and increasing NO_x (Fig. 5).

Fig. 6b refers to the Antarctic springtime (September-October): in this case the largest perturbation takes place in Cl-Br catalytic cycles for ozone destruction (up to $-1.0 \cdot 10^5 \text{ cm}^{-3} \text{ s}^{-1}$ at 50 hPa) and is due to the combination of increasing sulfate aerosol SAD, with decreasing NO_x and increasing Cl_x and Br_x , diabatic cooling and enhanced formation of PSCs as a consequence of the local temperature decrease and the availability of additional sulfate aerosol condensation nuclei, with a positive feedback on ozone loss frequencies [Tilmes *et al.*, 2009].

Figure 8 shows the latitude-altitude distribution of annually averaged ozone net production changes. The layer of increased ozone net production between 7 and 30 hPa (up to $+0.5 \cdot 10^5 \text{ cm}^{-3} \text{ s}^{-1}$) is due to the suppression of the NO_x cycle [Tie and Brasseur, 1995]. The layer of decreased ozone net production below 30 hPa (up to $-0.5 \cdot 10^5 \text{ cm}^{-3} \text{ s}^{-1}$) is due to a combination of reduced O_2 photolysis and enhanced HO_x and Cl-Br cycles due to the NO_x reduction. Negative changes above 7 hPa are produced by coupled changes of NO_x (Fig. 5) and of $O(^3P)$ from O_3 photolysis (Fig. 7b).

In the tropics, an important proportion of the ozone anomaly is caused by changes in upwelling due to perturbations of stratospheric heating rates [Tilmes *et al.*, 2009]. The heating from sulfate aerosols in the tropical middle stratosphere produces a temperature increase, which is mitigated by the ozone depletion in the same region. Anomalies of the global temperature at 70 hPa are shown in Fig. 9. GISS-E2-R simulates the smallest temperature anomaly. This is consistent with the smaller particle radius assumed in GISS-E2-R (see Table 2), which results in lower heating rates due to the smaller infrared absorption [Niemeier *et al.*, 2011]. It is also consistent with larger ozone depletion, hence cooling, due to the larger change in UV scattering and O_2 photolysis and to the absence of heterogeneous chemistry on sulfate aerosols. Figure 10 shows the simulated residual vertical velocity in the base case and its anomaly in G4 with respect to the base case. The models show a good consistency in the tropical upwelling and in the overall qualitative behavior of the G4 anomaly profile, with the magnitude of the largest relative increase of w^* between 20 and 30 km altitude (50 and 10 hPa), ranging between 2 to 5% for GISS-E2-R and MIROC-ESM-CHEM on one side, and 5 to 15% for ULAQ and GEOSCCM on the other side.

Figure 11 shows the vertical profiles of ozone changes in G4 at the tropics and mid-latitudes, as simulated by ULAQ-CCM, MIROC-ESM-CHEM and GEOSCCM; GISS-E2-R results are discussed separately (see ahead Fig. 12), since this model does not include the effects of the enhanced sulfate aerosol SAD on the heterogeneous chemistry. In the tropical region (Fig. 11a and 11b), ULAQ-CCM and MIROC-ESM-CHEM predict a decrease of ozone between 100 hPa and 50 hPa mostly due to changes in O_2 photolysis (Fig. 7a). GEOSCCM simulates no change below 70 hPa, being the aerosol feedback on photolysis rates absent in this model. From 70 to 30 hPa the ozone negative changes due to increased upwelling (Fig. 10) contribute the total ozone anomaly together with the enhanced chemical loss in HO_x , Cl_x and Br_x chemical cycles (Fig. 6a). The increased upwelling takes ozone poor air to ozone rich regions, creating the negative ozone anomaly that peaks at 30 hPa (-150 ppbv on average). Above 30 hPa the suppression of the NO_x cycle dominates the chemical perturbation (about +200 ppbv at 10 hPa), with GEOSCCM showing a wider altitude range of the negative ozone anomaly, due to the larger increase of upwelling in this model (Fig. 10). At mid-latitudes (Fig. 11c), where the effect on ozone of the increased upwelling disappears and the changes due to photolysis and heterogeneous chemistry dominate, GEOSCCM simulates smaller ozone anomalies with respect to ULAQ-CCM and MIROC-ESM-CCM.

The ozone tropical changes in GISS-E2-R are compared to ULAQ-CCM (run in this case without heterogeneous chemistry on sulfate aerosols) in Fig. 12. The left panel shows the ozone anomalies in G3: the smaller aerosol particles in GISS-E2-R with respect to ULAQ-CCM (Table 2) scatter more UV radiation, increasing the O_2 photolysis (Fig. 7). This effect, however, is balanced by the lower AOD calculated by GISS-E2-R (Fig. 1), and results in an ozone anomaly vertical profile similar to ULAQ-CCM nhc. In G4 (Fig. 12, right panel), where the sulfate injection burden is fixed by the experiment design, the AOD simulated by GISS-E2-R and ULAQ-CCM is similar, and the net results is a five times larger ozone depletion in GISS-E2-R than in ULAQ-CCM.

All models with heterogeneous chemistry simulate a significant ozone depletion in the Antarctic region (Fig. 13), due to a combination of increasing sulfate aerosol SAD (Fig. 13a) and enhanced formation of PSCs, produced in turn by local adiabatic and non-adiabatic cooling (Fig. 13b), the latter due to the feedback of photochemical ozone losses. ULAQ-CCM predicts the largest ozone depletion (Fig. 13c,d), both on annual basis and in springtime (-150 and -350 ppbv at 50 hPa, respectively). GEOSCCM simulates the smallest ozone depletion at 50 hPa during September-October, consistently with the

lower temperature anomaly and the absence of feedback between PSCs occurrence and changes in sulfate aerosol concentration in the GEOSCCM.

4.2 Column ozone changes and ozone radiative forcing

Globally, the injection of geoengineering aerosol leads in all models to a reduction of the ozone column for the central decade of experiments G3 and G4 (2040-2050) (see Table 3). The stratospheric aerosol suppresses the ozone depleting NO_x cycle, increasing ozone in the middle stratosphere, and enhances the ClO_x and OH_x cycles, decreasing ozone in the lower stratosphere [*Tie and Brasseur, 1995*].

Despite the constant stratospheric aerosol loading in G4, the magnitude of the geoengineering aerosol induced ozone depletion decreases in time (Fig. 14a) due to the decreasing atmospheric chlorine concentrations. ULAQ-CCM and MIROC-ESM-CHEM even simulates an increase in ozone starting from about 2050, when the ozone increase due to the suppression of the NO_x cycle is no longer balanced by the decrease in total column due to ClO_x and HO_x .

On the other hand, the models simulates an increasing magnitude of ozone depletion in G3 (Fig 14b). If no heterogeneous chemistry is included in the simulations (ULAQ-CCM nhc and GISS-E2-R nhc), the increasing stratospheric aerosol burden leads to a lower ozone net production during the whole simulated period because of photolysis and temperature changes. If the heterogeneous chemistry is included (ULAQ-CCM, dashed line in Fig 14b), the depletion of the ozone column is reduced after 2050, because of the increasing importance of NO_x relative to ClO_x . The net-adjusted tropopause radiative forcing (Tab. 3, Fig. 14d-e) is calculated off-line with the ULAQ-CCM radiative transfer code and its time behavior is closely correlated to that of the ozone column changes; it ranges between 0 and -0.1 W/m^2 (Fig. 14 d,e) except for the GISS-E2-R G4 case (not shown), where the O_3 column perturbation is larger (see Table 3 and discussion in section 4.2) and consequently the tropopause net adjusted RF raises to about -0.23 W/m^2 . These ozone RFs represents a rather small correction of the dominant direct forcing of geoengineering aerosols (about 2 to 10% of it). Table 3 suggests (as expected) that the largest contribution to the O_3 RF comes the stratospheric temperature adjustment in the longwave range [see *IPCC/TEAC, 2005*].

Through the depletion of the ozone column, the GeoMIP aerosols cause an increase in the global UV-B radiation reaching the surface (Fig. 15a). Such increase is, however, mostly over-compensated (in the tropics) by the scattering of UV-B radiation by the aerosols (Fig. 15b). The net effect on the surface UV-radiation is not meridionally uniform: while the tropics experience a decrease in UV-B radiation

reaching the surface, the UV-B over Arctic and Antarctic polar regions increases by about 5% with respect to the base case in 2040-2050, following the ozone column perturbation. These findings are in agreement with *Tilmes et al.* [2012], who found a decrease of 5% erythral UV in mid- and high latitudes for 2040 if the stratospheric halogen content from very short-lived halogen sources was considered. In these regions, the UV-B radiation changes are largely produced by the indirect ozone anomalies caused by geoengineering, but to a lesser extent also as direct consequence of the GeoMIP aerosols, which tend to increase the downward diffused radiation at large solar zenith angles [*Tsitas and Yung*, 1996]. A well tested radiative transfer model (TUV) [*Madronich and Floke*, 1998] has been used off-line for these UV-B calculations.

5. Conclusions

We have described the changes in ozone in simulations of GeoMIP experiments G3 and G4 in an ensemble of models. The results presented here are consistent with current understanding of the effects of different processes relevant to stratospheric ozone radiative, chemical, and dynamical effects.

In the tropics, ozone changes are a complex combination of reductions due to changes in photolysis rates, increases due to suppression of the NO_x cycle, reductions due to stratospheric heating and hence enhanced upwelling of ozone-poor air, and modulated reductions due to the addition of surfaces which serve as sites for heterogeneous chemistry. The net effect is a reduction of total column ozone in the tropics, which is enhanced in GISS-E2-R due to the lack of representation of heterogeneous chemistry, as well as a smaller aerosol size than was used in ULAQ-CCM.

In the mid-latitudes, upwelling of ozone-poor air does not play a dominant role, so photolysis changes and heterogeneous chemistry dominate. GEOSCCM does not include photolysis changes, and as such, shows smaller changes in lower stratospheric ozone and total column.

At the poles, particularly the Antarctic, cooling induced by photochemical ozone losses and circulation changes resulting from stratospheric heating enhances polar stratospheric cloud formation, thus promoting ozone depletion. The net effect is a reduction in polar ozone by over 5% in the majority of model simulations.

The presence of a heterogeneous chemistry parameterization increases the importance of NO_x relative to ClO_x . As ClO_x availability is reduced, depletion of the ozone column also lessens. In two models,

the globally averaged ozone column increases after the year 2050. In models which include heterogeneous chemistry, total ozone column changes are small (1-2 DU) and ozone radiative forcing is less than 0.1 W m^{-2} . As such, with the exception of polar regions, which show significant increases in UV-B, models predict small impacts on total column stratospheric ozone as simulated in the two experiments presented here.

These results are potentially heavily dependent upon the experimental design. ULAQ-CCM is the only model included in this study which can represent aerosol microphysical growth; it shows a substantial increase in sulfate aerosol effective radius, consistent with past studies [Heckendorn *et al.*, 2009; English *et al.*, 2012]. A larger aerosol size reduces the radiative efficiency of the aerosols, requiring much more sulfate aerosol mass to achieve the desired radiative forcing [Pierce *et al.*, 2010]. Therefore, the effects on ozone described here may be magnified, depending upon the required mass of SO_2 to meet a climate goal. Moreover, these results are likely specific to continuous tropical injections. Modulating the latitudinal and temporal distribution of geoengineering could have different climate effects [MacMartin *et al.*, 2013].

The results presented here would benefit from further uniformization of the experiment design. Although we have identified particular processes that impact the results, we have not been able to isolate the effects of the processes. For example, all models used different aerosol size distributions. It is known that larger particles have a greater infrared effect but a smaller surface area, so inhomogeneous representations of the aerosol size distribution confound changes in ozone due to the radiative or dynamical effects and changes due to heterogeneous chemistry. Obtaining robust features in a more controlled setting could be a useful follow-up study.

The results presented here show only one aspect of geoengineering with stratospheric aerosols when conducted in a certain way. We do not advocate deployment of geoengineering, nor do we suggest ways in which it would be performed. Such decisions should be reserved for legitimate governance structures. Moreover, decisions regarding geoengineering should not be made based solely on physical science studies. Social, political, economic, and ethical perspectives also have an important role in informing decisions about geoengineering.

Acknowledgments

We thank all participants of the Geoengineering Model Intercomparison Project and their model development teams, CLIVAR/WCRP Working Group on Coupled Modeling for endorsing GeoMIP, and the scientists managing the Earth System Grid data nodes who have assisted with making GeoMIP output available. We acknowledge the World Climate Research Programme's Working Group on Coupled Modelling, which is responsible for CMIP, and we thank the climate modeling groups for producing and making available their model output. For CMIP the U.S. Department of Energy's Program for Climate Model Diagnosis and Intercomparison provides coordinating support and led development of software infrastructure in partnership with the Global Organization for Earth System Science Portals. Ben Kravitz is supported by the Fund for Innovative Climate and Energy Research (FICER). The Pacific Northwest National Laboratory is operated for the U.S. Department of Energy by Battelle Memorial Institute under contract DE-AC05-76RL01830. Simulations performed by Ben Kravitz and Valentina Aquila were supported by the NASA High-End Computing (HEC) Program through the NASA Center for Climate Simulation (NCCS) at Goddard Space Flight Center. Valentina Aquila is supported by the NASA MAP program.

The authors acknowledge use of SAGE-II data for stratospheric aerosols.

SW was supported by the SOUSEI program, MEXT, Japan and the simulations were conducted using the Earth Simulator.

References

- Aquila, V., L. D. Oman, R. S. Stolarski, P. R. Colarco, and P. A. Newman (2012), Dispersion of the volcanic sulfate cloud from a Mount Pinatubo-like eruption, *J. Geophys. Res.*, *117*, D06216. doi:10.1029/2011JD016968.
- Aquila, V., L. D. Oman, R. Stolarski, A. R. Douglass, and P. A. Newman (2013), The Response of Ozone and Nitrogen Dioxide to the Eruption of Mt. Pinatubo at Southern and Northern Midlatitudes, *J. Atmos. Sci.*, *70*(3), 894–900. doi:10.1175/JAS-D-12-0143.1.
- Bingen, C., D. Fussen, and F. Vanhellemon (2004), A global climatology of stratospheric aerosol size distribution parameters derived from SAGE II data over the period 1984-2000: 1. Methodology and climatological observations, *J. Geophys. Res.*, *109*(D6), D06201. doi:10.1029/2003JD003518.

- Bluth, G. J. S., S. D. Doiron, C. C. Schnetzler, A. J. Krueger, and L. S. Walter (1992), Global tracking of the SO₂ clouds from the June , 1991 Mount Pinatubo eruptions, *Geophys. Res. Lett.*, *19*, 151-154.
- Brasseur, G., and C. Granier (1992), Mount Pinatubo Aerosols, Chlorofluorocarbons, and Ozone Depletion, *Science*, *257*(5074), 1239–1242.
- Budyko, M. I. (1974), *Climate and life*, Academic Press, New York, 508 pp.
- Carslaw, K. S., B. P. Luo, and T. Peter (1995), An analytic expression for the composition of aqueous HNO₃–H₂SO₄ stratospheric aerosols including gas phase removal coupled HNO₃, *Geophys. Res. Lett.*, *22*, 1877–1880, doi:10.1029/95GL01668.
- Chipperfield, M. and Q. Liang, et al. (2013), SPARC Assessment on Atmospheric Lifetimes, Chapter 5: Model Estimates of Lifetimes, *in press*.
- Chin, M., R. B. Rood, S.-J. Lin, and J.-F. Müller (2000), Atmospheric sulfur cycle simulated in the global model GOCART: Model description and global properties. *J. Geophys. Res.*, *105*(D20), 24671–24687. doi:10.1029/2000JD900384.
- Chou, M.-D., and M. J. Suarez (1999), A solar radiation parameterization for atmospheric studies, NASA Tech. Rep., TM-1999-104606, 50 pp., NASA Goddard Space Flight Cent., Greenbelt, MD.
- Chou, M.-D., M. J. Suarez, X.-Z. Liang, and M. M.-H. Yan (2001), A thermal infrared radiation parameterization for atmospheric studies, NASA Tech. Rep., TM-2001-104606, 68 pp., NASA Goddard Space Flight Cent., Greenbelt, MD.
- Colarco, P., A. Da Silva, M. Chin, and T. Diehl (2010), Online simulations of global aerosol distributions in the NASA GEOS-4 model and comparisons to satellite and ground-based aerosol optical depth, *J. Geophys. Res.*, *115*(D14), D14207. doi:10.1029/2009JD012820.
- Crutzen, P. J. (2006), Albedo enhancement by stratospheric sulfur injections: A contribution to resolve a policy dilemma? *Climatic Change*, *77*(3–4), 211-220, doi:10.1007/s10584-006-9101-y.
- Dahlback, A., and K. Stamnes (1991), A new spherical model for computing the radiation field available for photolysis and heating at twilight, *Planet. Space Sci.*, *39*, 671-683.

- Deshler, T., D. J. Hofmann, B. J. Johnson, and W. R. Rozier (1992), Balloonborne measurements of the Pinatubo aerosol size distribution and volatility and Laramie, Wyoming during the summer of 1991, *Geophys. Res. Lett.*, *19*(2), 199-202, doi:10.1029/91GL02787.
- English, J., O. B. Toon, and M. J. Mills (2012), Microphysical simulations of sulfur burdens from stratospheric sulfur geoengineering, *Atmos. Chem. Phys.*, *12*, 4775-4793, doi:10.5194/acp-12-4775-2012.
- Eyring, V., et al. (2006), Assessment of temperature, trace species, and ozone in chemistry-climate model simulation of the recent past, *J. Geophys. Res.*, *111*, D22308, doi:10.1029/2006JD007327, 2006.
- Eyring, V., et al. (2008), Overview of the new CCMVal reference and sensitivity simulations in support of upcoming ozone and climate assessments and the planned SPARC CCMVal Report. SPARC Newsletter, No. 30, World Climate Research Program, Geneva, Switzerland, 20–26.
- Fahey, D. W., et al. (1993), *In situ* measurements constraining the role of sulphate aerosols in mid-latitude ozone depletion, *Nature*, *363*, 509-514.
- Gent, P. R., G. Danabasoglu, L. J. Donner, M. M. Holland, E. C. Hunke, S. R. Jayne, D. M. Lawrence, et al. (2011), The Community Climate System Model Version 4, *J. Clim.*, *24*(19), pp. 4973–4991, doi: 10.1175/2011JCLI4083.
- Grant, W. B., J. Fishman, E. V. Browell, V. G. Brackett, D. Nganga, A. Minga, B. Cros, R. E. Veiga, C. F. Butler, M. A. Fenn, and G. D. Nowicki (1992), Observations of reduced ozone concentrations in the tropical stratosphere after the eruption of Mt. Pinatubo, *Geophys. Res. Lett.*, *19*, 1109-1112.
- Hansen, J. E., A. Lacis, R. Ruedy, and M. Sato (1992), Potential climate impact of Mount Pinatubo eruption, *Geophys. Res. Lett.*, *19*, 215-218.
- Hanson, D. and K. Mauersberger (1988), Laboratory studies of the nitric acid trihydrate: Implications for the south polar stratosphere, *Geophys. Res. Lett.*, *15*, 855–858, doi:10.1029/GL015i008p00855.
- Heckendorn P., et al. (2009), The impact of geoengineering aerosols on stratospheric temperature and ozone, *Env. Res. Lett.*, *4*, 045108, doi:10.1088/1748-9326/4/4/045108.

- Hendricks J., B. Kärcher, and U. Lohmann (2011), Effects of ice nuclei on cirrus clouds in a global climate model, *J. Geophys. Res.*, *116*, D18206, doi:10.1029/2010JD015302.
- IPCC/TEAC *Special Report on Safeguarding the Ozone Layer and the Global Climate System: Issues Related to Hydrofluorocarbons and Perfluorocarbons*. Prepared by Working Group I and III of the Intergovernmental Panel on Climate Change, and the Technology and Economic Assessment Panel, Metz B. et al. Eds., Cambridge University Press, Cambridge, United Kingdom and New York, NY, USA, 488 pp., 2005.
- Johnston, P. V., R. L. McKenzie, J. G. Keys, and W. A. Matthews (1992), Observations of depleted stratospheric NO₂ following the Pinatubo volcanic eruption, *Geophys. Res. Lett.*, *19*(2), 211–213.
- Jones, A., *et al.* (2013), The “termination effect” in experiment G2 of the Geoengineering Model Intercomparison Project (GeoMIP), *J. Geophys. Res.*, submitted.
- Kärcher, B., and U. Lohmann (2002), A parameterization of cirrus cloud formation: homogeneous freezing of supercooled aerosols, *J. Geophys. Res.*, *107*, 4010, 10.1029/2001JD000470.
- Kinne, S., O. B. Toon, and M. J. Prather (1992), Buffering of stratospheric circulation by changing amounts of tropical ozone: A Pinatubo case study, *Geophys. Res. Lett.*, *19*, 1927–1930.
- Kirchner, I., G. L. Stenchikov, H.-F. Graf, A. Robock, and J. C. Antuna (1999), Climate model simulation of winter warming and summer cooling following the 1991 Mount Pinatubo volcanic eruption, *J. Geophys. Res.*, *104*, 19039–19055.
- Koch, D., G. A. Schmidt, and C. V. Field (2006), Sulfur, sea salt, and radionuclide aerosols in GISS ModelE, *J. Geophys. Res.*, *111*, D06206, doi:10.1029/2004JD005550.
- Koike, M., N. B. Jones, W. A. Matthews, P. V. Johnston, R. L. McKenzie, D. Kinnison, and J. Rodriguez (1994), Impact of Pinatubo aerosols on the partitioning between NO₂ and HNO₃, *Geophys. Res. Lett.*, *21*(7), 597. doi:10.1029/94GL00303.
- Koster, R. D., M. J. Suarez, A. Ducharne, M. Stieglitz, and P. Kumar (2000), A catchment-based approach to modeling land surface processes in a general circulation model: 1. Model structure, *J. Geophys. Res.*, *105*(D20), 24,809–24,822, doi:10.1029/2000JD900327.

- Kravitz, B., A. Robock, O. Boucher, H. Schmidt, K. E. Taylor, G. Stenchikov, and M. Schulz (2011a), The Geoengineering Model Intercomparison Project (GeoMIP), *Atm. Sci. Lett.*, *12*, 162-167, doi:10.1002/asl.316.
- Kravitz, B., A. Robock, O. Boucher, H. Schmidt, and K. E. Taylor (2011b), Specifications for GeoMIP experiments *G1* through *G4* (Version 1.0), available online at http://climate.envsci.rutgers.edu/GeoMIP/docs/specificationsG1_G4_v1.0.pdf.
- Kravitz, B., et al. (2013), Climate model response from the Geoengineering Model Intercomparison Project (GeoMIP), *J. Geophys. Res.*, submitted.
- Labitzke, K., and M.P. McCormick (1992), Stratospheric temperature increases due to Pinatubo aerosols, *Geophys. Res. Lett.*, *19*, 207-210.
- Lacis, A., J. E. Hansen, and M. Sato (1992), Climate forcing by stratospheric aerosols, *Geophys. Res. Lett.*, *19*, 1607-1610.
- Lambert, A., R. G. Grainger, J. J. Remedios, C. D. Rodgers, M. Corney, and F. W. Taylor (1993), Measurements of the evolution of the Mt. Pinatubo aerosol cloud by ISAM, *Geophys. Res. Lett.*, *20*, 1287-1290.
- Lin, S.-J. (2004), A “vertically Lagrangian” finite-volume dynamical core for global models, *Mon. Weather Rev.*, *132*, 2293–2307, doi:10.1175/1520-0493(2004)132<2293:AVLFDC>2.0.CO;2.
- Lock, A. P., A. R. Brown, M. R. Bush, G. M. Martin, and R. N. B. Smith (2000), A new boundary layer mixing scheme. Part I: Scheme description and single-column model tests, *Mon. Weather Rev.*, *128*, 3187–3199, doi:10.1175/1520-0493(2000)128<3187:ANBLMS>2.0.CO;2.
- Long, C. S., and L. L. Stowe (1994), Using the NOAA/AVHRR to study stratospheric aerosol optical thickness following the Mt. Pinatubo eruption, *Geophys. Res. Lett.*, *21*, 2215-2218.
- Louis, J., M. Tiedtke, and J. Geleyn (1982): A short history of the PBL parameterization at ECMWF, paper presented at ECMWF Workshop on Planetary Boundary Layer Parameterization, Eur. Cent. for Medium- Range Weather Forecasts, Reading, U. K.

- MacMartin, D. G., D. W. Keith, B. Kravitz, and K. Caldeira (2013), Managing trade-offs in geoengineering through optimal choice of non-uniform radiative forcing, *Nature Climate Change*, 3, 365-368, doi:10.1038/nclimate1722.
- Madronich, S., and S. Flocke (1998), The role of solar radiation in atmospheric chemistry. In *Handbook of Environmental Chemistry*, P. Boule (Ed.), Springer, Heidelberg, pp. 1-26.
- McCormick, M. P. and R. E. Veiga (1992), SAGE II measurements of early Pinatubo aerosols, *Geophys. Res. Lett.*, 19, 155-158.
- McCormick, M. P., L. W. Thomason, and C. R. Trepte (1995), Atmospheric effects of the Mt. Pinatubo eruption, *Nature*, 373, 399-404.
- Meinshausen, M., et al. (2011), The RCP greenhouse gas concentrations and their extensions from 1765 to 2300, *Climatic Change*, 109, 213-241, doi:10.1007/s10584-011-0156-z.
- Minschwaner, K., R. J. Salawitch, and M. B. McElroy (1993), Absorption of Solar Radiation by O₂: Implications for O₃ and Lifetimes of N₂O, CFCl₃, and CF₂Cl₂, *J. Geophys. Res.*, 98, 10,543–10,561, doi:10.1029/93JD00223.
- Molod, A., L. Takacs, M. Suarez, J. Bacmeister, I.-S. Song, and A. Eichmann (2012), The GEOS-5 Atmospheric General Circulation Model: Mean Climate and Development from MERRA to Fortuna. Technical Report Series on Global Modeling and Data Assimilation, 28.
- Moorthi, S., and M. J. Suarez (2012), Relaxed Arakawa-Schubert. A parameterization of moist convection for general circulation models, *Mon. Weather Rev.*, 120, 978–1002, doi:10.1175/1520-0493(1992)120<0978: RASAPO>2.0.CO;2.
- Morgenstern, O., et al. (2010), A review of CCMVal-2 models and simulations, *J. Geophys. Res.*, 115, D00M02, doi:10.1029/2009JD013728.
- Niemeier, U., H. Schmidt, and C. Timmreck (2011), The dependency of geoengineered sulfate aerosol on the emission strategy, *Atmos. Sci. Lett., Special Issue: Geoengineering*, 12(2), 189–194.
- Pawson, S., R. S. Stolarski, A. R. Douglass, P. A. Newman, J. E. Nielsen, S. M. Frith, and M. L. Gupta (2008), Goddard Earth Observing System chemistry-climate model simulations of stratospheric

ozone-temperature coupling between 1950 and 2005, *J. Geophys. Res.*, *113*(D12), D12103. doi:10.1029/2007JD009511.

Petters, M. D., and S. M. Kreidenweis (2007), A single parameter representation of hygroscopic growth and cloud condensation nucleus activity, *Atmos. Chem. Phys.*, *7*(8), 1961–1971.

Pierce, J. R., D. K. Weisenstein, P. Heckendorn, T. Peter, and D. W. Keith (2010), Efficient formation of stratospheric aerosol for climate engineering by emission of condensible vapor from aircraft, *Geophys. Res. Lett.*, *37*(18), L18805, doi:10.1029/2010GL043975.

Pitari, G. (1993), A numerical study of the possible perturbation of stratospheric dynamics due to Pinatubo aerosols: Implications for tracer transport, *J. Atmos. Sci.*, *50*, 2443–2461.

Pitari, G., and V. Rizi (1993), An estimate of the chemical and radiative perturbation of stratospheric ozone following the eruption of Mt. Pinatubo, *J. Atmos. Sci.*, *50*, 3260–3276.

Pitari, G., and E. Mancini (2002), Short-term climatic impact of the 1991 volcanic eruption of Mt. Pinatubo and effects on atmospheric tracers, *Nat. Hazards Earth Syst. Sci.*, *2*, 91–108. doi:10.5194/nhess-2-91-2002.

Pitari G., E. Mancini, V. Rizi, and D. T. Shindell (2002), Impact of Future Climate and Emission Changes on Stratospheric Aerosols and Ozone, *J. Atmos. Sci.*, *59*.

Prather, M.J. (1992), Catastrophic loss of stratospheric ozone in dense volcanic clouds, *J. Geophys. Res.*, *97*, 10187–10191.

Randles, C. A., et al. (2013), Intercomparison of shortwave radiative transfer schemes in global aerosol modeling: Results from the AeroCom Radiative Transfer Code Experiment, *Atmos. Chem. Phys.*, *13*, 2347–2379, doi:10.5194/acp-13-2347-2013.

Rayner, N. A., D. E. Parker, E. B. Horton, C. K. Folland, L. V. Alexander, D. P. Rowell, E. C. Kent, and A. Kaplan (2003), Global analyses of sea surface temperature, sea ice, and night marine air temperature since the late nineteenth century, *J. Geophys. Res.*, *108*(D14), 4407, doi:10.1029/2002JD002670.

Read, W. G., L. Froidevaux, and J.W. Waters (1993), Microwave limb sounder measurements of stratospheric SO₂ from the Mt. Pinatubo volcano, *Geophys. Res. Lett.*, *20*, 1299–1302.

- Rienecker, M. M., M. J. Suarez, R. Gelaro, R. Todling, J. Bacmeister, E. Liu, et al. (2011), MERRA: NASA's Modern-Era Retrospective Analysis for Research and Applications, *J. Clim.*, *24*(14), 3624–3648. doi:10.1175/JCLI-D-11-00015.1.
- Robock, A. (2000), Volcanic eruptions and climate, *Rev. Geophys.*, *38*, 191-219, doi:10.1029/1998RG000054.
- Robock, A., L. Oman, and G. L. Stenchikov (2008), Regional climate responses to geoengineering with tropical and Arctic SO₂ injections, *J. Geophys. Res.*, *113*, D16101, doi:10.1029/2008JD010050.
- Russell, G. L., J. R. Miller, and D. Rind (1995), A coupled atmosphere-ocean model for transient climate change. *Atmos.-Ocean*, *33*, 683-730.
- Sato, M., J. E. Hansen, M. P. McCormick and J. B. Pollack (1993), Stratospheric aerosol optical depth, 1850–1990, *J. Geophys. Res.*, *98*, 22987–22994, doi:10.1029/93JD02553.
- Schmidt, G. A., et al. (2006), Present-day atmospheric simulations using GISS ModelE: Comparison to in situ, satellite and reanalysis data, *J. Clim.*, *19*, 153–192, doi:10.1175/JCLI3612.1.
- Schoeberl, M. R., P. K. Bhartia, and E. Hilsenrath (1993), Tropical ozone loss following the eruption of Mt. Pinatubo, *Geophys. Res. Lett.*, *20*, 29-32.
- Shepherd, J., et al. (2009), Geoengineering the climate: Science, governance, and uncertainty, Royal Society Policy document 10/09, 82 pp.
- Soden, B. J., R. T. Wetherald, G. L. Stenchikov, and A. Robock (2002), Global cooling after the eruption of Mount Pinatubo: A test of climate feedback by water vapor, *Science*, *296*(5568), 727-730, doi:10.1126/science.296.5568.727.
- Stenchikov, G. L., I. Kirchner, A. Robock, H.-F. Graf, J. C. Antuna, R. Grainger, A. Lambert, and L. Thomason (1998), Radiative forcing from the 1991 Mt. Pinatubo volcanic eruption, *J. Geophys. Res.*, *103*, 13837-13858.
- Stieglitz, M., A. Ducharme, R. Koster, and M. Suarez (2001), The impact of detailed snow physics on the simulation of snow cover and subsurface thermodynamics at continental scales, *J. Hydrometeorol.*, *2*(3), 228–242, doi:10.1175/1525-7541(2001)002<0228:TIODSP>2.0.CO;2.

- Strahan, S. E., et al. (2011), Using transport diagnostics to understand Chemistry Climate Model ozone simulations *J. Geophys. Res.*, *116*, D17302, doi: 10.1029/2010JD015360.
- Tang, I. N. (1996), Chemical and size effects of hygroscopic aerosols on light scattering coefficients, *J. Geophys. Res.*, *101*, D14, 19245-19250.
- Taylor, K. E., R. J. Stouffer, and G. A. Meehl (2012), An Overview of CMIP5 and the Experiment Design, *Bull. Amer. Meteor. Soc.*, *93*, 485–498. doi: <http://dx.doi.org/10.1175/BAMS-D-11-00094.1>.
- Thomason, L. W., G. S. Kent, C. R. Trepte, and L. R. Poole (1997a), A comparison of the stratospheric aerosol background periods of 1979 and 1989–1991. *J. Geophys. Res.*, *102* (D3), 3611–3616, doi: 10.1029/96JD02960.
- Thomason, L. W., L. R. Poole, and T. Deshler (1997b), A global climatology of stratospheric aerosol surface area density deduced from stratospheric aerosol and gas experiment II measurement: 1984–1994, *J. Geophys. Res.*, *102*, D7, 8967–8976, doi: 10.1029/96JD02962.
- Tie, X., and G. Brasseur (1995), The response of stratospheric ozone to volcanic eruptions: Sensitivity to atmospheric chlorine loading. *Geophys. Res. Lett.*, *22*(22), 3035–3038. doi:10.1029/95GL03057.
- Tilmes, S., R. Müller, and R. Salawitch (2008), The sensitivity of polar ozone depletion to proposed geoengineering schemes, *Science*, *320*(5880), 1201–1204, doi:10.1126/science.1153966.
- Tilmes, S., R. R. Garcia, D. E. Kinnison, A. Gettelman, and P. J. Rasch (2009), Impact of geoengineered aerosols on the troposphere and stratosphere, *J. Geophys. Res.*, *114*(D12). doi:10.1029/2008JD011420.
- Tilmes, S., D.E. Kinnison, R.R. Garcia, R. Salawitch, T. Canty, J. Lee-Taylor, S. Madronich, and K. Chance (2012), Impact of very short-lived halogens on stratospheric ozone abundance and UV radiation in a geo-engineered atmosphere, *Atmos. Chem. Phys.*, *12*, 10945–10955 doi:10.5194/acp-12-10945-2012.
- Toon, O. B., C. P. McKay, T. P. Ackerman, and K. Santhanam (1989), Rapid Calculation of Radiative Heating Rates and Photodissociation Rates in Inhomogeneous Multiple Scattering Atmospheres, *J. Geophys. Res.*, *94*, 16,287–16,301, doi:10.1029/JD094iD13p16287.

- Trepte, C.R., and M.H. Hitchman (1992), Tropical stratospheric circulation deduced from satellite aerosol data, *Nature*, 355, 626-628.
- Tsitas, S. R., and Y. L. Yung (1996), The effect of volcanic aerosols on ultraviolet radiation in Antarctica, *Geophys. Res. Lett.*, 23, 157-160.
- Watanabe, S., et al. (2011a), MIROC - ESM; model description and basic results of CMIP5 - 20c3m experiments, *Geosci. Model Dev. Discuss.*, 4, 1063-1128, doi:10.5194/gmdd-4-1063-2011.
- Watanabe, S., et al. (2011b), Future projections of surface UV - B in a changing climate, *J. Geophys. Res.*, 116, D16118, doi:10.1029/2011JD015749.
- Weisenstein, D., S. Bekki, G. Pitari, C. Timmreck, and M. Mills (2006), *WCRP/SPARC scientific assessment of stratospheric aerosol properties*; Chapter 6: Modeling of stratospheric aerosols, L. Thomason and Th. Peter Eds., WCRP-124, WMO/TD-1295, SPARC report #4.
- Young, R.E., H. Houben, and O. B. Toon (1994), Radiatively forced dispersion of the Mt. Pinatubo volcanic cloud and induced temperature perturbations in the stratosphere during the first few months following the eruption, *Geophys. Res. Lett.*, 21, 369-372.

Tables

Table 1. Summary of model runs (nhc = no heterogeneous chemistry on sulfate aerosols).

	RCP4.5	G3	G3-nhc	G4	G4-nhc
ULAQ-CCM	2	2	2	2	2
GISS-E2-R	3		3		3
MIROC-ESM-CHEM	1			4	
GEOSCCM	2			2	

Table 2. Stratospheric aerosol effective radius (μm) at 20 km over the tropics (2040-2050). For the observations, an average over 1999-2000 is used for the unperturbed background and over April 1992-March 1993 for a volcanic perturbation (i.e. Pinatubo) comparable in magnitude to G4 (in terms of average stratospheric mass burden of sulfate; see text). Background aerosol is not included in RCP4.5 simulations with GEOSCCM (see Section 2.4 for details)

	RCP4.5	G3	G4
ULAQ-CCM	0.19	0.48	0.61
GISS-E2-R	0.15	0.35	0.35
MIROC-ESM-CHEM	0.24		0.24
GEOSCCM	*		0.61
SAGE-II	0.22 \pm 0.02		0.59 \pm 0.02

Table 3. O₃ column changes with respect to base case (DU); shortwave, longwave, adjusted longwave and net adjusted tropopause radiative forcing (mW/m^2) of ozone; surface UV-B change (percent) due to ozone changes. Annually and globally averaged values for the whole decade 2040-2050.

	O ₃ col (DU)	RF-O ₃ SW (mW/m^2)	RF-O ₃ LW (mW/m^2)	RF-O ₃ LWadj (mW/m^2)	RF-O ₃ NET (mW/m^2)	Surface UV-B change (%)
G4 – RCP4.5 ULAQ-CCM	-1.1	2.0	-16.5	-34.1	-32.1	0.06
G4 – RCP4.5 MIROC-ESM-CHEM	-1.1	8.8	-11.1	-44.4	-35.6	0.22
G4 – RCP4.5 GEOSCCM	-2.1	9.8	-19.1	-37.4	-27.6	0.51
G3 – RCP4.5 ULAQ-CCM	-2.8	4.4	-58.9	-96.8	-92.4	1.16
G4 nhc – RCP4.5 ULAQ-CCM	-1.9	21.6	-32.8	-64.5	-42.9	0.88
G4 nhc – RCP4.5 GISS-E2-R	-9.7	127	-23.6	-361	-234	3.23
G3 nhc – RCP4.5 ULAQ-CCM	-1.9	22.7	-29.5	-60.9	-38.2	0.81

G3 nhc – RCP4.5 GISS-E2-R	-2.1	31.7	-7.5	-61.8	-30.1	0.69
------------------------------	------	------	------	-------	-------	------

Figure captions

Fig. 1abcde. Time series of globally averaged stratospheric AOD at 0.55 μm in the models: 1960-2000 (top panel (a)) and G3, G4 perturbed cases in 2020-2070 (mid panels (b) and (c) respectively). Bottom panels (d), (e) show the zonally averaged AOD change with respect to RCP4.5, in G3 and G4, respectively. Line styles for the models are specified in the legend.

Fig. 2ab. Vertical profiles of aerosol extinction ratio between 0.525 μm and 1.020 μm wavelength channels in the tropics (20S-20N), as calculated in the ULAQ-CCM for case G4 (solid line, 2040-2050 average), for the Pinatubo case (dashed line, April 1992 – March 1993), and for background conditions (dash-dotted line, 1996-2000), compared to SAGE II retrievals (triangles and asterisks for 1992/1993 and 1999/2000 conditions, respectively) (panel a). Panel (b): Aerosol size distribution (dn/dlogr , cm^{-3}) calculated in the ULAQ model and averaged over the tropics and in the 30-70 hPa vertical layer (2040-2050). Solid line is for RCP4.5; dashed line is for case G4.

Fig. 3abc. Sulfate aerosol surface area density ($\mu\text{m}^2/\text{cm}^3$) calculated in the models (ULAQ-CCM, MIROC-ESM-CHEM, GEOSCCM) for background conditions (1996-2000 average) and compared to SAGE-II data (asterisks). Panels (a,b,c) refer to tropics (20S-20N), mid-latitudes (30S-50S, 30N-50N) and polar regions (60S-90S, 60N-90N), respectively.

Fig. 4abc. As in Fig. 3, but for but for case G4 (2040-2050 average). An indirect comparison is made with SAGE-II data for post-Pinatubo conditions (April 1992 – March 1993 average; triangles). The average sulfate mass loading above the tropopause is comparable in the latter case with respect to G4. The stratospheric mass burden comparison in these two cases is made using averages from ULAQ-CCM and GEOSCCM time-dependent simulations (4.83 ± 0.06 Tg-S for April 1992 – March 1993 post-Pinatubo conditions and 4.7 ± 0.6 Tg-S for G4).

Fig. 5ab. $\text{NO}+\text{NO}_2$ mixing ratio changes, as calculated in ULAQ-CCM, MIROC-ESM-CHEM and GEOSCCM (2040-2050). Panel (a) is for the tropics; panel (b) for mid-latitudes.

Fig. 6ab. ULAQ-CCM calculated changes of net ozone production terms ($10^5 \text{ mol cm}^{-3} \text{ s}^{-1}$) in G4 with respect to RCP4.5 (2040-2050); see legend for the different curves. Panel (a) is for the annual mean over the tropics (20S-20N); panel (b) is for the October mean over south polar latitudes (65S-90S).

Fig. 7abc. Calculated percent changes of O_2 and $\text{O}_3 \rightarrow \text{O}(^3\text{P})$ photodissociation coefficients in panels (a) and (b), respectively, for G4 with respect to base case (tropics, spring equinox). A fixed O_3 vertical profile (RCP4.5) is used in all cases, in order to evaluate the photodissociation sensitivity to the aerosol perturbation. Only the solid-circle line in panel (a) shows the JO_2 perturbation (in the ULAQ-CCM) with both aerosol and O_3 changes taken into account in G4.

Fig. 8. As in Fig. 6b, but for zonally averaged values of the total net production.

Fig. 9ab. Panel (a): time series of calculated global temperature changes at 50 hPa, for G4 with respect to base case from 2020 to 2070 (K); solid, dashed, dash-dotted and dotted-circles line are for ULAQ-CCM, GISS-E2-R MIROC-ESM-CHEM and GEOSCCM, respectively. Panel (b): as above, but for ULAQ-CCM temperature anomalies from 1960 to 2000 relative to the 1980-1989 average compared to observations. Solid/dashed lines are with/without volcanic aerosol stratospheric heating, respectively. Observations are from sondes and ERA-40 reanalysis (solid line with diamonds) (Eyring et al., 2006).

Fig. 10ab. Residual vertical velocity w^* in the tropical stratosphere (mm/s) (average 15S-15N, 2040-2050) for baseline conditions in panel (a) and percent changes G4-BC in panel (b). ULAQ-CCM,

GISS-E2-R, MIROC-ESM-CHEM and GEOSCCM and results are shown with solid, dashed, dash-dotted and dotted-circles line, respectively.

Fig. 11abc. Calculated ozone profile changes in G4 with respect to base case (2040-2050). Panel (a) is for tropical mixing ratio (ppbv); panel (b) for tropical number concentration (10^{12} cm^{-3}); panel (c) for mid-latitude number concentration (10^{12} cm^{-3}).

Fig. 12ab. As in Fig. 12b, but for G3 and G4 in panels (a) and (b), respectively, both without heterogeneous chemistry on sulfuric acid aerosols.

Fig. 13abcd. G4-RCP4.5 changes averaged over the South Polar region (65S-90S) for 2040-2050. Top panels (a,b) are for aerosol surface area density ($\mu\text{m}^2/\text{cm}^3$) and temperature (K), respectively (annual mean). Bottom panels (c,d) are for ozone mixing ratio (ppbv), annual and September-October mean values, respectively. Solid, dash-dotted and dotted-circles line are for ULAQ-CCM, MIROC-ESM-CHEM and GEOSCCM, respectively.

Fig. 14abcde. Top panels (a, b): time series of global O_3 column changes in G4, G3, respectively, with respect to the base case (DU), averaged per decade. Mid panel (c): zonally and time averaged column ozone changes (2040-2050) with respect to RCP4.5. Bottom panels (d, e): as in panels (a, b), but for net adjusted tropopause RF (mW/m^2). Line styles for the models are specified in the legend.

Fig. 15ab. Zonally averaged UV-B percent changes at the surface, due to ozone and aerosol perturbations in G3, G4, with respect to RCP4.5 (average 2040-2050). Results for the different models are shown in top panel (a), with line styles as specified in the legend. A model average of the results is shown in the bottom panel (b), with dashed line for UV-B changes due to ozone perturbations only, dash-dotted line for aerosol perturbations only, solid line for the total.

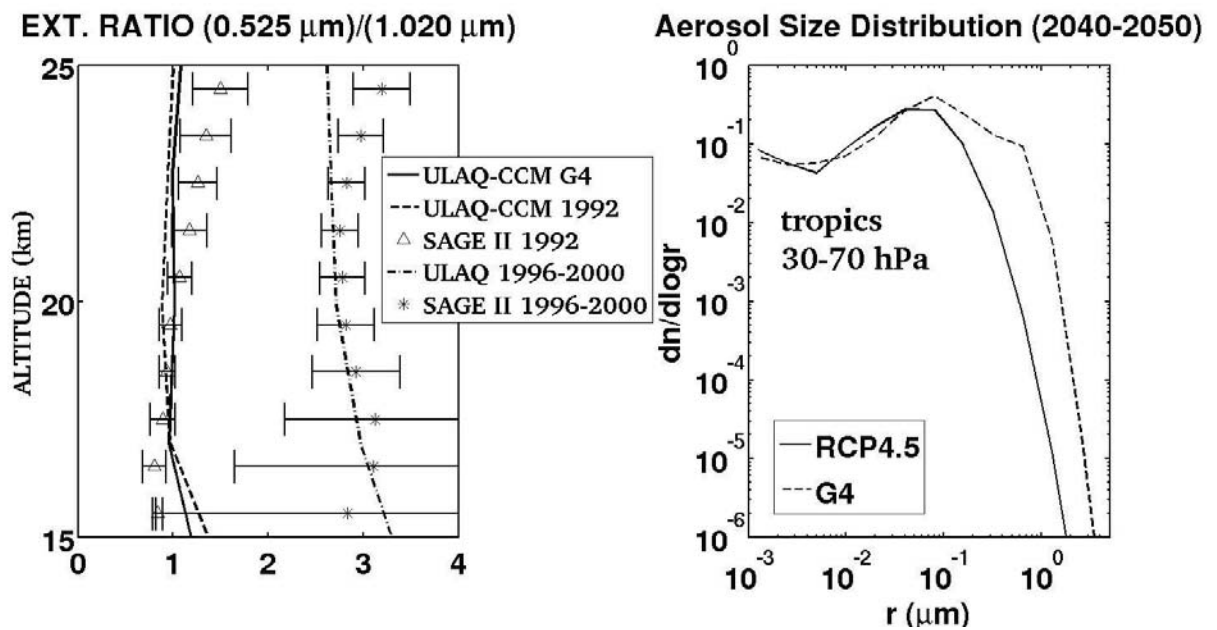


Fig. 2ab. Vertical profiles of aerosol extinction ratio between $0.525 \mu\text{m}$ and $1.020 \mu\text{m}$ wavelength channels in the tropics (20S-20N), as calculated in the ULAQ-CCM for case G4 (solid line, 2040-2050 average), for the Pinatubo case (dashed line, May 1992 – April 1993), and for background conditions (dash-dotted line, 1999-2000), compared to SAGE II retrievals (triangles and asterisks for 1992/1993 and 1999/2000 conditions, respectively) (panel a). Panel (b): Aerosol size distribution (dn/dlogr , cm^{-3}) calculated in the ULAQ model and averaged over the tropics and in the 30-70 hPa vertical layer (2040-2050). Solid line is for RCP4.5; dashed line is for case G4.

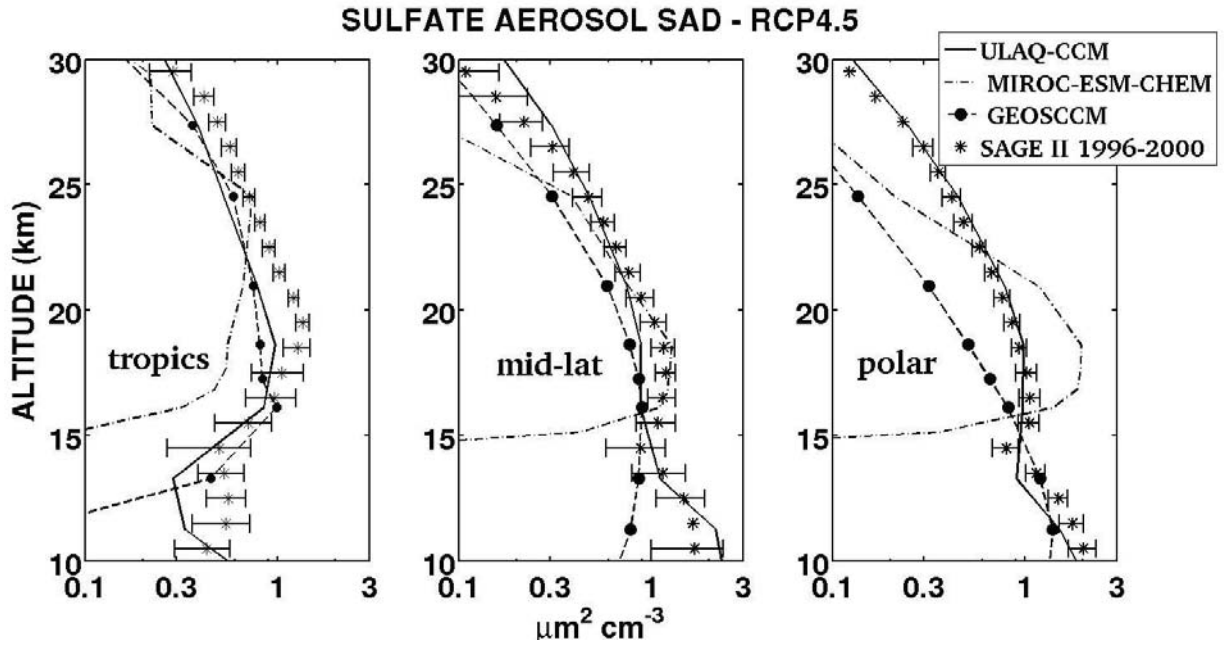


Fig. 3abc. Sulfate aerosol surface area density ($\mu\text{m}^2/\text{cm}^3$) calculated in the models (ULAQ-CCM, MIROC-ESM-CHEM, GEOSCCM) for background conditions (1996-2000 average) and compared to SAGE-II data (asterisks). Panels (a,b,c) refer to tropics (20S-20N), mid-latitudes (30S-50S, 30N-50N) and polar regions (60S-90S, 60N-90N), respectively.

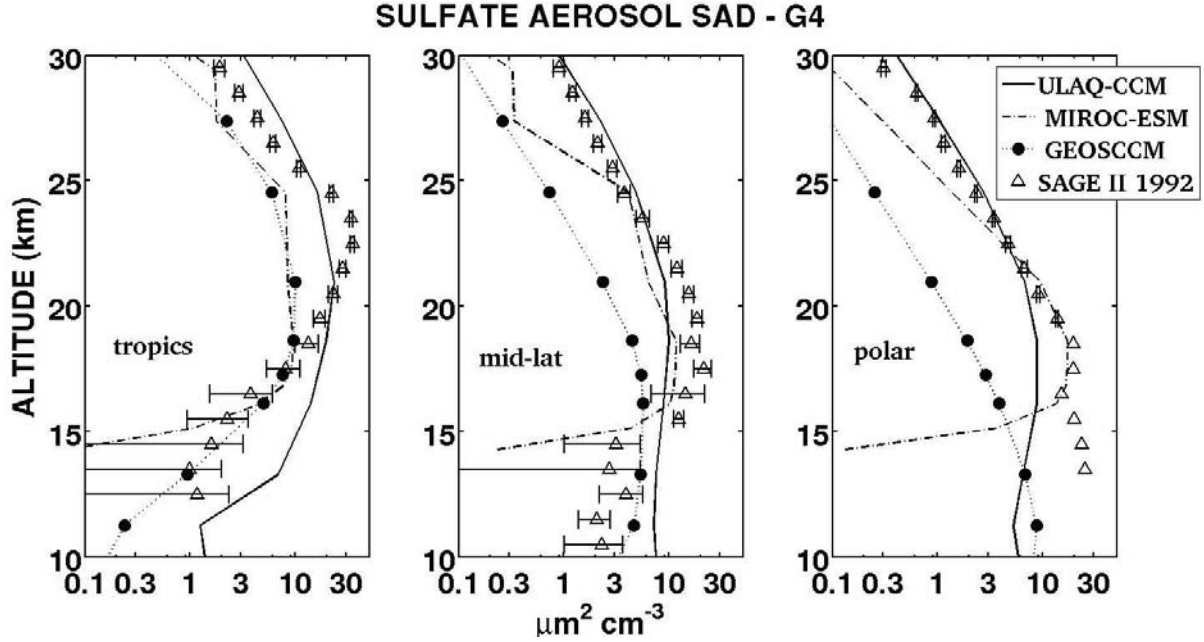


Fig. 4abc. As in Fig. 3, but for case G4 (2040-2050 average). An indirect comparison is made with SAGE-II data for post-Pinatubo conditions (April 1992 – March 1993 average; triangles), when the average sulfate mass loading above the tropopause is comparable to G4 (4.83 ± 0.06 Tg-S for April 1992 – March 1993 post-Pinatubo conditions and 4.7 ± 0.6 Tg-S for G4, average of ULAQ-CCM and GEOSCCM time-dependent simulations).

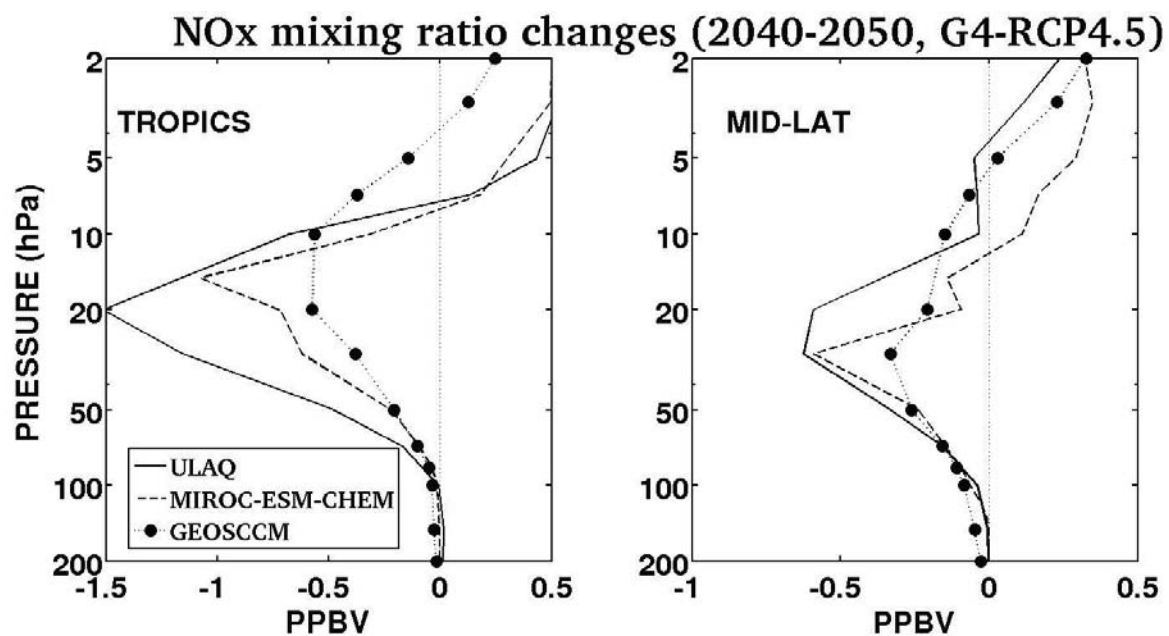


Fig. 5ab. NO+NO₂ mixing ratio changes, as calculated in ULAQ-CCM, MIROC-ESM-CHEM and GEOSCCM (2040-2050). Panel (a) is for the tropics (20S-20N); panel (b) for mid-latitudes (30S-50S, 30N-50N).

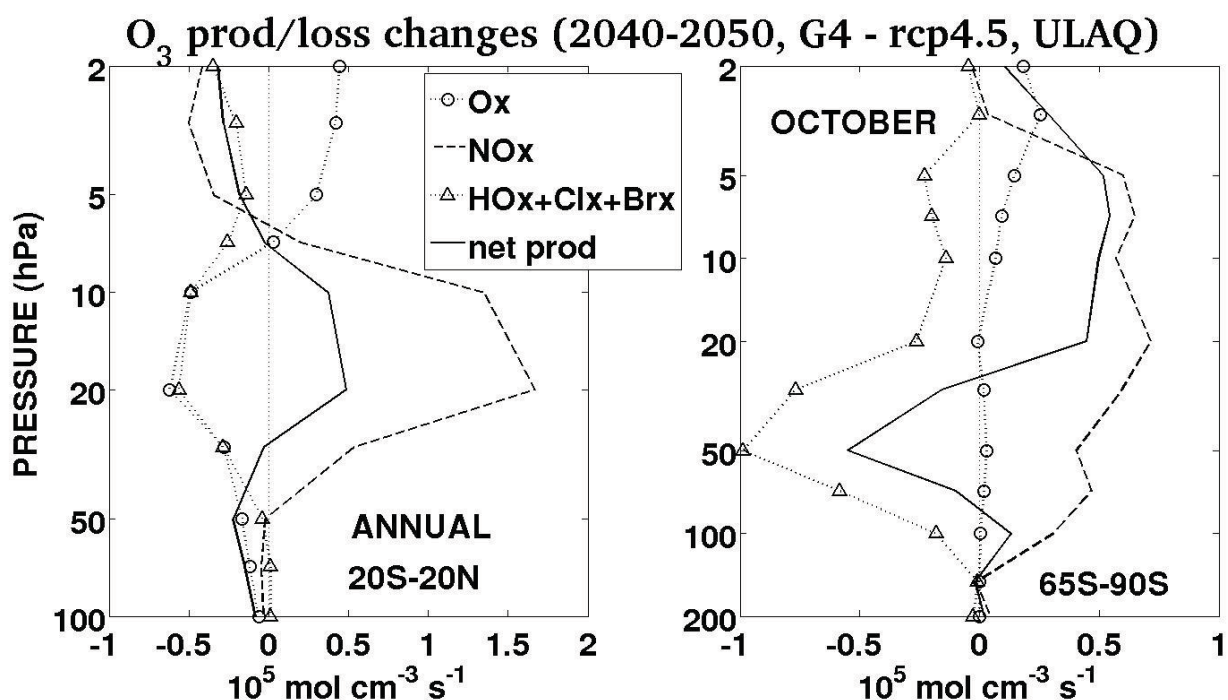


Fig. 6ab. ULAQ-CCM calculated changes of net ozone production terms ($10^5 \text{ mol cm}^{-3} \text{ s}^{-1}$) in G4 with respect to RCP4.5 (2040-2050); see legend for the different curves. Panel (a) is for the annual mean over the tropics (20S-20N); panel (b) is for the October mean over south polar latitudes (65S-90S).

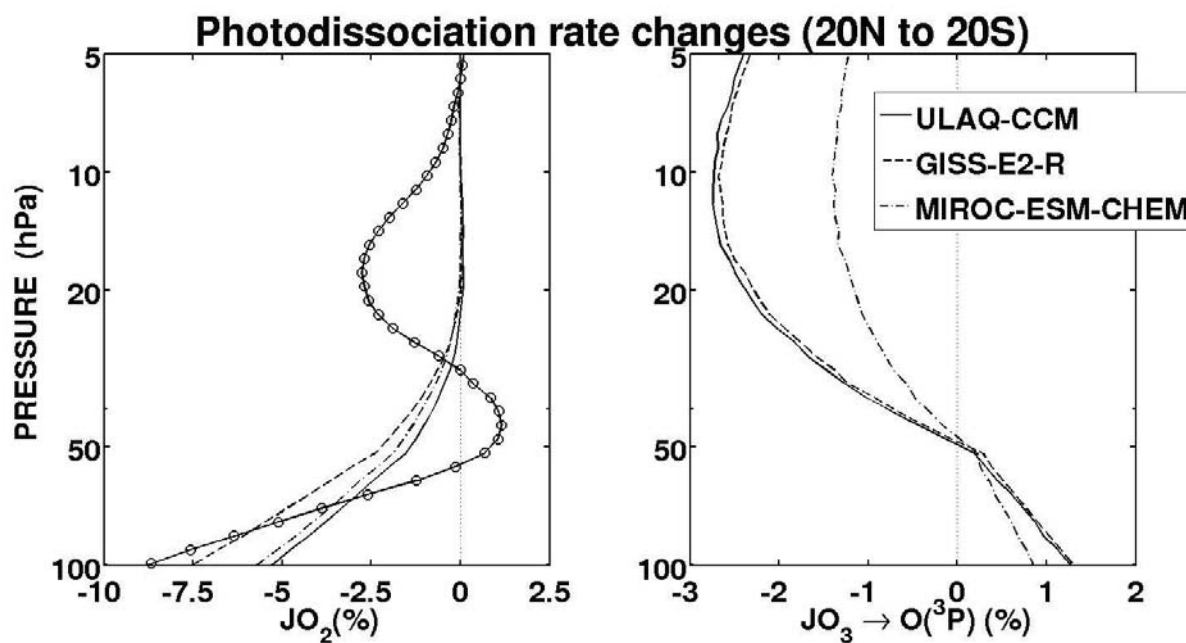


Fig. 7ab. Calculated percent changes of O_2 (panel a) and $O_3 \rightarrow O(^3P)$ (panel b) photodissociation coefficients for G4 with respect to base case (tropics, spring equinox). A fixed O_3 vertical profile (RCP4.5) is used in all cases except for the solid-circle line, in order to evaluate the photodissociation sensitivity to the aerosol perturbation. The solid-circle line in panel (a) shows the JO_2 perturbation (in the ULAQ-CCM) with both aerosol and O_3 changes taken into account in G4.

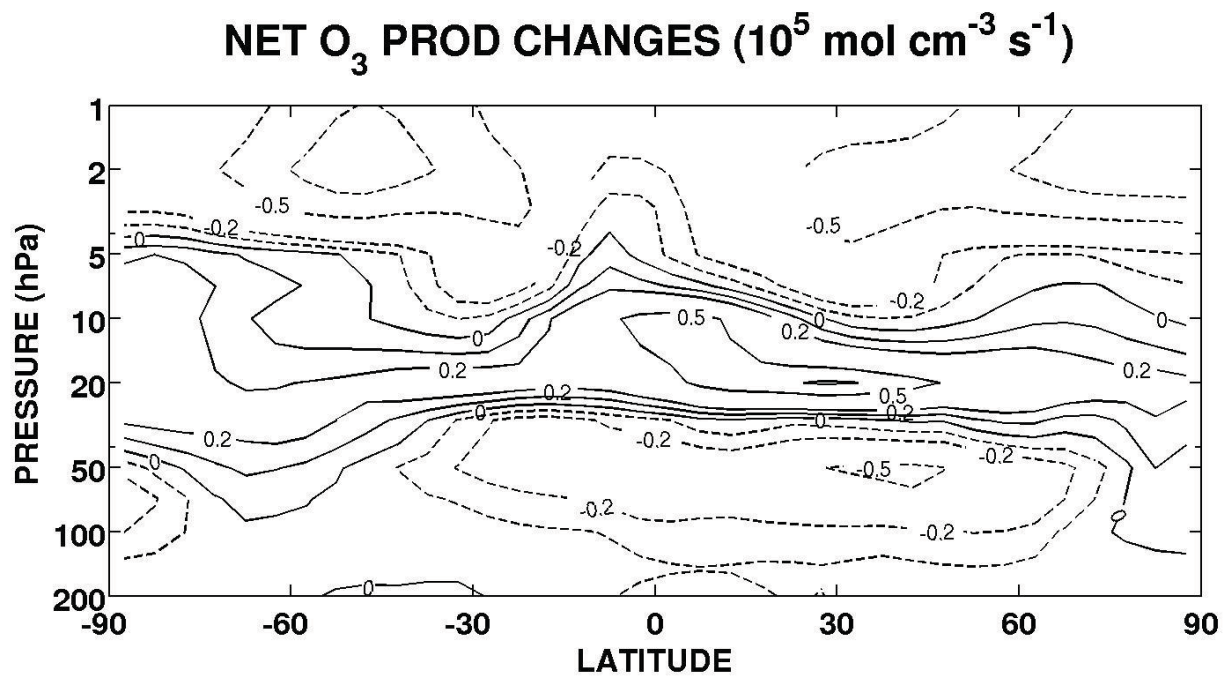


Fig. 8. As in Fig. 6b, but for zonally averaged values of the total net production.

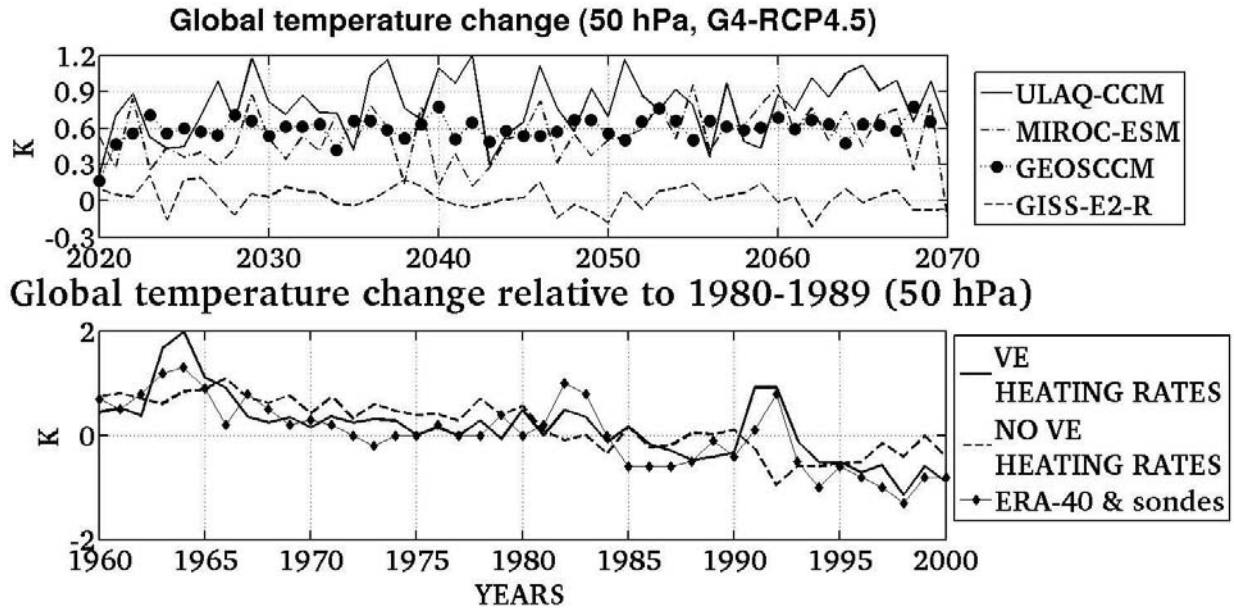


Fig. 9ab. Panel (a): time series of calculated global temperature changes at 50 hPa, for G4 with respect to base case from 2020 to 2070 (K); solid, dashed, dash-dotted and dotted-circles line are for ULAQ-CCM, GISS-E2-R MIROC-ESM-CHEM and GEOSCCM, respectively. **Panel (b):** as above, but for ULAQ-CCM temperature anomalies from 1960 to 2000 relative to the 1980-1989 average compared to observations. Solid/dashed lines are with/without stratospheric heating from volcanic aerosol, respectively. Observations are from sondes and ERA-40 reanalysis (solid line with diamonds) (Eyring et al., 2006).

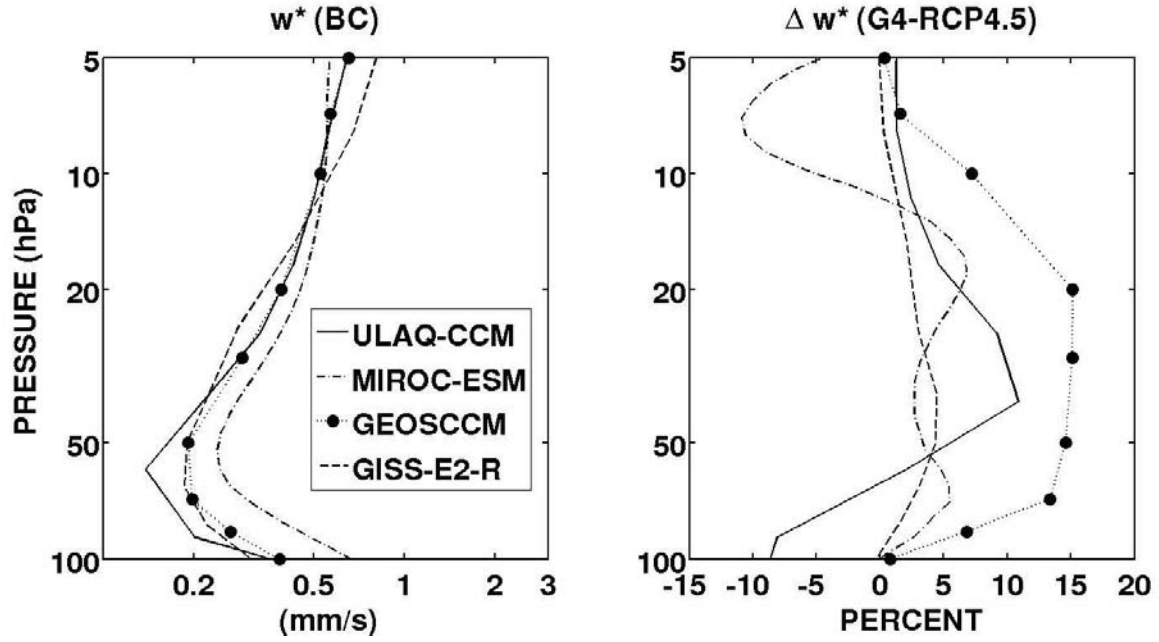


Fig. 10ab. Residual vertical velocity w^* in the tropical stratosphere (mm/s) (average 15S-15N, 2040-2050) for baseline conditions in panel (a) and percent changes G4-BC in panel (b). ULAQ-CCM, GISS-E2-R, MIROC-ESM-CHEM and GEOSCCM and results are shown with solid, dashed, dash-dotted and dotted-circles line, respectively.

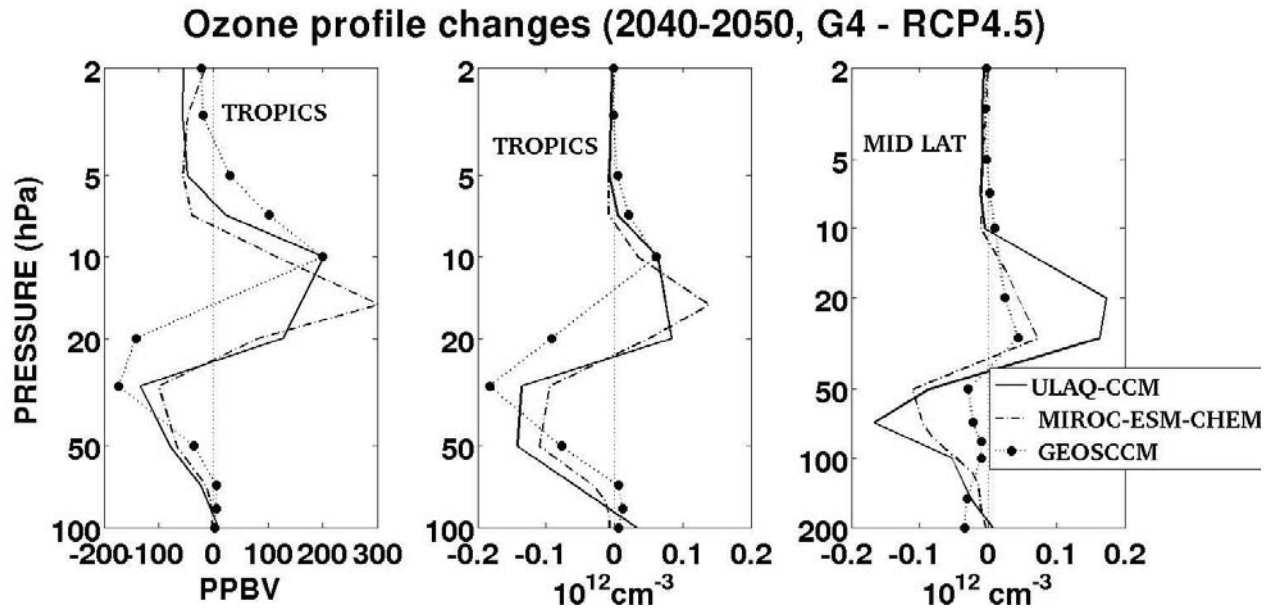


Fig. 11abc. Calculated ozone profile changes in G4 with respect to base case (2040-2050). Panel (a) is for tropical mixing ratio (ppbv); panel (b) for tropical number concentration (10^{12} cm^{-3}); panel (c) for mid-latitude number concentration (10^{12} cm^{-3}).

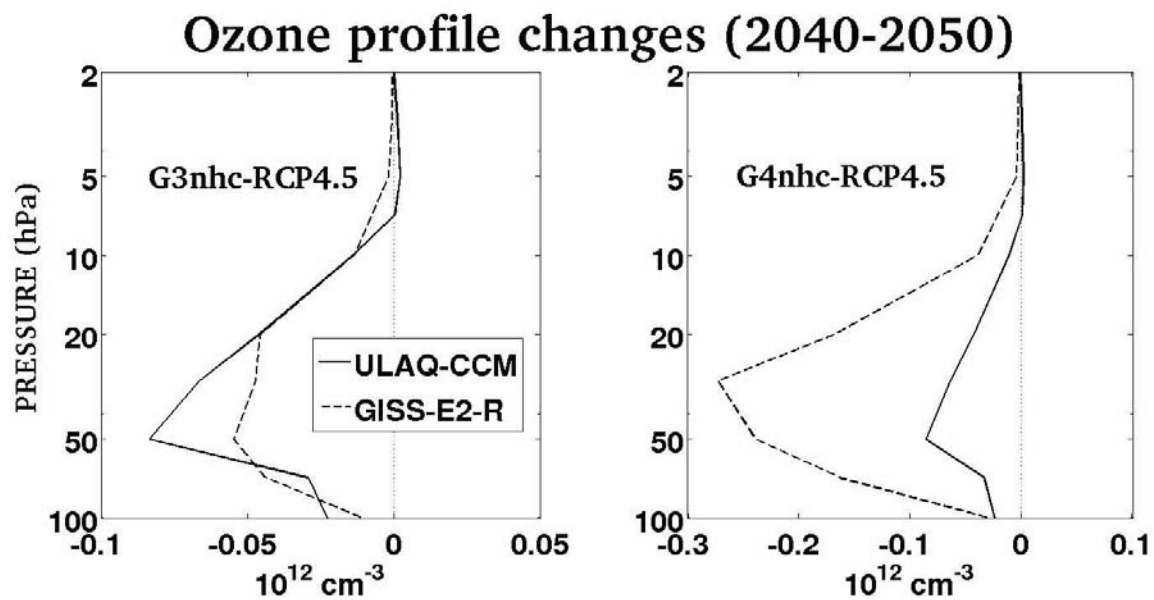


Fig. 12ab. As in Fig. 12b, but without heterogeneous chemistry on sulfuric acid aerosols for G3 and G4 in panels (a) and (b), respectively.

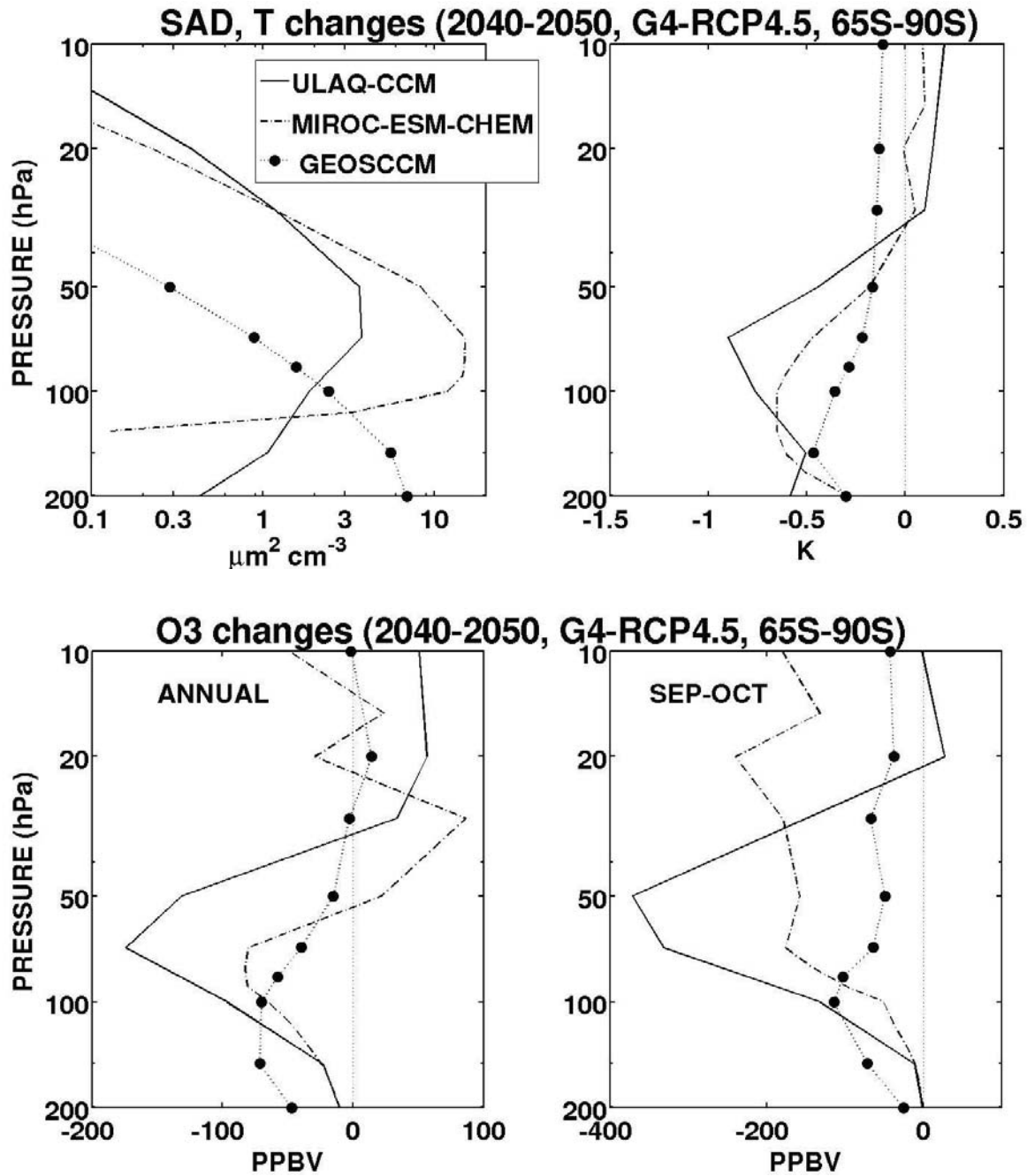


Fig. 13abcd. G4-RCP4.5 changes averaged over the South Polar region (65S-90S) for 2040-2050. Top panels (a,b) are for aerosol surface area density ($\mu\text{m}^2/\text{cm}^3$) and temperature (K), respectively (annual mean). Bottom panels (c,d) are for ozone mixing ratio (ppbv), annual and September-October mean values, respectively. Solid, dash-dotted and dotted-circles line are for ULAQ-CCM, MIROC-ESM-CHEM and GEOSCCM, respectively.

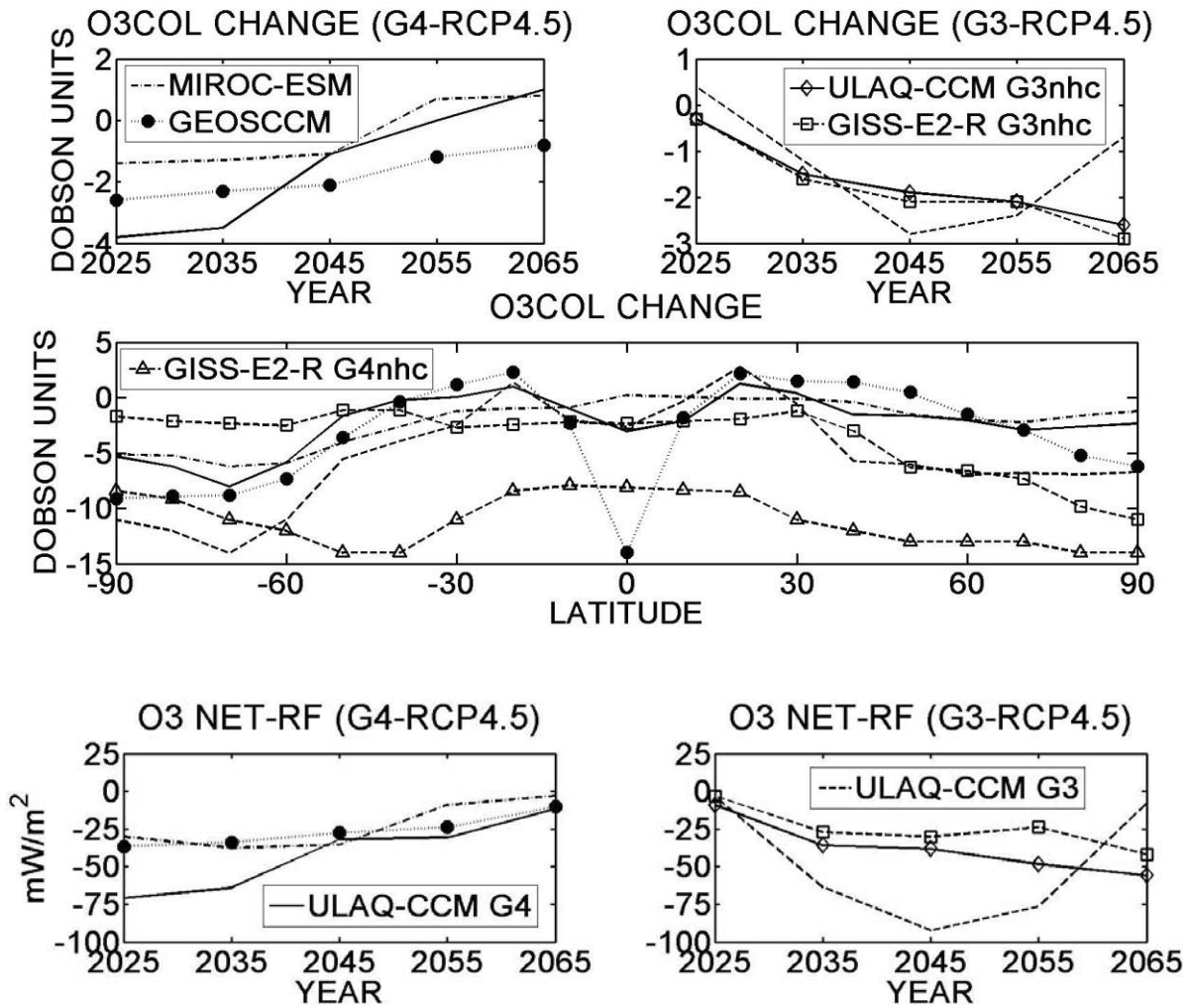


Fig. 14abcde. Top panels (a, b): time series of global O₃ column changes in G4, G3, respectively, with respect to the base case (DU), averaged per decade. Mid panel (c): zonally and time averaged column ozone changes (2040-2050) with respect to RCP4.5. Bottom panels (d, e): as in panels (a, b), but for net adjusted tropopause RF (mW/m²). Line styles for the models are specified in the legend.

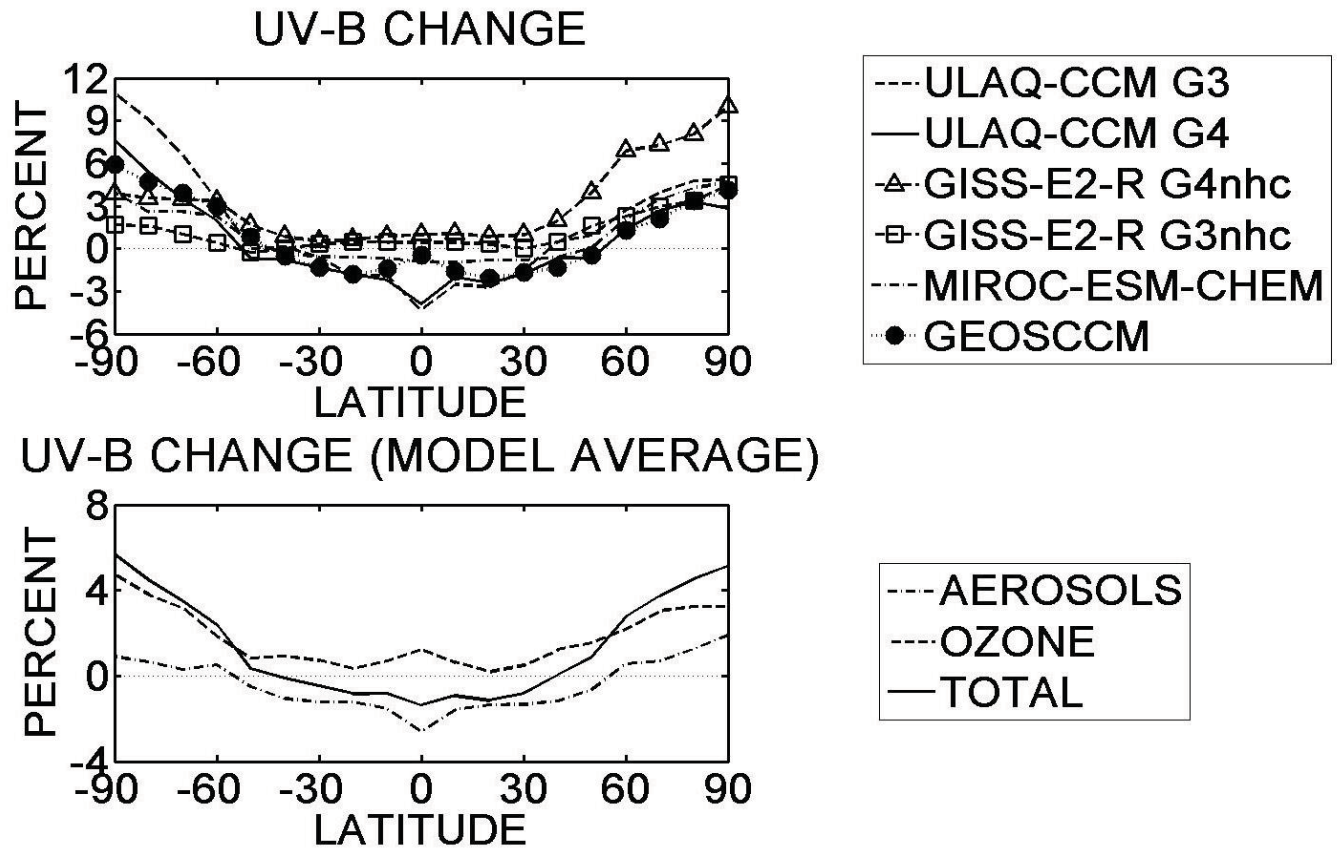


Fig. 15ab. Zonally averaged UV-B percent changes at the surface, due to ozone and aerosol perturbations in G3, G4, with respect to RCP4.5 (average 2040-2050). Results for the different models are shown in top panel (a), with line styles as specified in the legend. A model average of the results is shown in the bottom panel (b), with dashed line for UV-B changes due to ozone perturbations only, dash-dotted line for aerosol perturbations only, solid line for the total.